Self-Intersecting Marginally Outer-Trapped Surfaces within Spherically Symmetric Black Holes

by

A thesis submitted to the

School of Graduate Studies

in partial fulfilment of the

requirements for the degree of

Master of Science

Department of Physics and Physical Oceanography

Memorial University of Newfoundland

April 2023

St. John's   Newfoundland

Statement of Contributions

Part of chapter 3 and the entirety of chapter 4 is based on:

- R. A. Hennigar, K. T. B. Chan, L. Newhook, and I. Booth, "Interior marginally outer trapped surfaces of spherically symmetric black holes," Phys. Rev. D 105, 044024 (2022).

  Author's contributions: KTB was co-primary investigator for section III and the founder of the phenomenon investigated in section IV. KTB developed the numerical process outlined in subsection II.D. and wrote approximately 60% of subsection II.D. KTB produced nine of the seventeen figures (figures 2, 4, 7, 9, 10, 11, 12, 13, 14) and provided approximately 70% of the data that are displayed in all figures excluding figures 3, 6, and 8.

Abstract

Black hole mergers have been studied for over 50 years but are still not fully understood, despite growing relevance with the constant stream of gravitational wave detections. Due to the non-linearity of Einstein's theory of gravity, it is difficult to draw an analytical solution. Numerical simulations of the merger process have progressed and are now able to discern the dynamics of two black hole horizons eventually becoming one, with the involvement of exotic self-intersecting surfaces. Further study has shown that these self-intersecting surfaces appear not only in the dynamical case of black hole mergers, but also for static black holes. This manuscript provides a background to the advancement of our understanding of black hole mergers, discovery of these self-intersecting surfaces, and our advancement in understanding these self-intersecting surfaces through their analysis inside different black holes.

Acknowledgements

I would like to acknowledge the territory in which the Memorial University of Newfoundland and Labrador, St. John's campus, is located as the ancestral homelands of the Beothuk, and the island of Newfoundland as the ancestral homelands of the Mi'kmaq and Beothuk. I would also like to recognize the Inuit of Nunatsiavut and NunatuKavut and the Innu of Nitassinan, and their ancestors, as the original people of Labrador.

Completion of this thesis would not have been possible alone. I submit this having had a network of people supporting me academically and socially throughout the past three years. I will now acknowledge these people. Dr. Robie A. Hennigar has been an aspiring figure for my well-being. I have Robie to thank for my understanding in the *physics* of black holes. As for the *geometry* and *mathematics* aspects, I owe those skills to my M.Sc. supervisor Dr. Ivan Booth. Taking his chances on this Calgary-obsessed immigrant, Ivan facilitated the development of my public inquisitive behaviour and helped me realize the researcher I strive to become. My parents, William K. Sievers and Nuchsuporn Sievers. Yen-Shyun "Sean" Huang for the 14+ years of continuing friendship, whom I speak my mind to at the freest capacity. Liam Bussey, my academic twin who was my rival in our Alberta versus Newfoundland & Labrador and physics versus mathematics discussions, pushed me academically as I pushed them. Haruka Yoshino, for without whom I would have not completed the thesis in such a timely manner if at all. Finally, the gravity group at MUN and the faculty & graduate students in the physics and mathematics departments, namely: Drs. Graham Cox, Stephanie Curnoe, Hari Kunduri, and Marco Merkli.

Contents

List of Figures

List of Abbreviation and Symbols

Geometrized units $(G = c = 1)$ are used. The MTW sign convention $(-+++)$ will be followed for the metric. Greek indices $(\alpha, \beta, \gamma, \ldots)$ will run over 4-dimensional spacetime coordinates, lower-case roman indices $(a, b, c, \ldots)$ over 3-dimensional spatial coordinates, and upper-case roman indices $(A, B, C, \ldots)$ over 2-dimensional spatial coordinates. The Einstein summation convention will be employed: $w_\alpha v^\alpha \equiv \sum_{\alpha=0}^{4} w_\alpha v^\alpha$. Vectors are written with a raised index and coordinate directions often written as partial derivatives: $v^a = (-1, 2, 0)^T = -\hat{x} + 2\hat{y} \implies v^a \frac{\partial}{\partial x^a} = -\frac{\partial}{\partial x} + 2\frac{\partial}{\partial y}$. One-forms (co-vectors) have a lowered index v_a and are related to their corresponding vectors through the metric $v_a = g_{ab} v^b$.

Symbol	Description
x^α, y^α	(3+1)-D spacetime coordinates $\{$e.g. $x^0 = t, x^1 = x, x^2 = y, x^3 = z\}$
x^a, y^a	3-D spatial coordinates
x^A, y^A	2-D spatial coordinates
$g_{\alpha\beta}$	Metric tensor
g	Determinant of the metric tensor $\det(g_{\alpha\beta})$
$R_{\alpha\beta\gamma\sigma}$	Riemann curvature tensor
$R_{\alpha\beta}$, R	Ricci tensor and Ricci curvature scalar

Chapter 1

Introduction

It should no longer be a surprise that black holes exist. Having been only a mathematical consequence of Einstein's theory of general relativity for the past century [1], recent findings show evidence of such densely packed objects at our galactic centre [2, 3] and at the centre of a neighbouring galaxy [4]. The nomenclature itself is perfect for describing a region that eternally imprisons any that dares enter, isolating such violators from the rest of the universe[1].

Newton's law of gravity, which postulates that it be a fundamental force between two masses,

$$\vec{F}_{\text{Newton}} = \frac{m_1 m_2}{r^2} \hat{r} \ , \tag{1.1}$$

allows for modelling of everyday gravitational effects (such as the free-fall trajectory of an apple) and extends as far as orbital mechanics, as demonstrated by the seminal work of Kepler. Errors arise around that scale, such as the precession of the perihelion of Mercury's orbit. The need for a more accurate theory of gravity to model

---

[1]This nomenclature is elaborated through dialogue in [5, pg. 872-875].

the extremities was called for, which Albert Einstein would answer. With the arrival of Einstein's postulates and theory of special relativity, the extension for curved spacetimes would become Einstein's theory of general relativity [6]. This new regime opens up possibilities including our global positioning system, the bending of light, and black holes. Einstein's theory relates geometry and matter, implying that motion due to gravity is a consequence of geometry.

The action functional [7, pg. 122] for general relativity reads[2]

$$S = \int_{\mathcal{M}} \sqrt{-g} \left(\frac{1}{16\pi} R - \mathcal{L}_M \right) \mathrm{d}^4 x \ , \tag{1.2}$$

where g is the determinant of the metric tensor $\det(g_{\alpha\beta})$, R the Ricci curvature scalar, and $\mathcal{L}_M$ the Lagrangian associated with the matter field living on this manifold $\mathcal{M}$. It is important to note that many different coordinates characterized by the metric tensor $g_{\alpha\beta}$ can be placed upon a manifold $\mathcal{M}$ (all related through coordinate transformations). The choice of coordinates leaves the theory invariant as the Ricci curvature scalar is invariant under coordinate transformations. Extremizing this action, the Einstein field equations result:

$$R_{\alpha\beta} - \frac{1}{2} R \ g_{\alpha\beta} = 8\pi T_{\alpha\beta} \ , \tag{1.3}$$

where $T_{\alpha\beta}$ is the stress-energy tensor from the matter fields described by the associated Lagrangian $\mathcal{L}_M$: $\quad T_{\alpha\beta} \equiv -2\frac{\partial \mathcal{L}_M}{\partial g^{\alpha\beta}} + \mathcal{L}_M g_{\alpha\beta}$. Eqn (1.3) explicitly states the relationship between geometry (on the left-hand side) and matter (on the right-hand side), and we interpret this tangle as geometry telling the matter how to move while the matter tells the geometry how to curve. Although there exists higher-dimensional manifolds

---

[2]For our purposes of discussing GR, we omit details about the evaluation of the action involving the boundary $\partial \mathcal{M}$ terms, and instead only consider the action on the bulk $\mathcal{M}$.

that satisfy higher-dimensional versions of Einstein's equations, this manuscript will focus solely on $(3+1)$-dimensional spacetimes (three spatial dimensions taking on the positive sign in the metric and one temporal dimension taking the negative, following the $-+++$ signature).

A trivial vacuum ($T_{\alpha\beta} = 0$) solution to these field equations (1.3) is the (flat) Minkowski spacetime: $\eta_{\alpha\beta}\mathrm{d}x^\alpha\mathrm{d}x^\beta = -\mathrm{d}t^2 + \mathrm{d}x^2 + \mathrm{d}y^2 + \mathrm{d}z^2$. Shortly after Einstein's realization of GR, a non-trivial vacuum solution was discovered by Karl Schwarzschild with a metric tensor ($g_{\alpha\beta}$) that reads

$$g_{\alpha\beta}\mathrm{d}x^\alpha\mathrm{d}x^\beta = -\left(1 - \frac{2M}{r}\right)\mathrm{d}t^2 + \frac{\mathrm{d}r^2}{1 - \frac{2M}{r}} + r^2\mathrm{d}\Omega^2 \ . \tag{1.4}$$

The solid 2-sphere $\mathrm{d}\Omega^2 = \mathrm{d}\theta^2 + \sin^2\theta\,\mathrm{d}\phi^2$ follows the physics radial-coordinate convention with polar angle $\theta \in [0, \pi]$ and azimuthal angle $\phi \in [0, 2\pi)$.

This solution is Ricci flat $R_{\alpha\beta} = 0 \implies R = 0$ and thus satisfies the vacuum field equations. In these particular coordinates, the metric characterizes the gravitational field outside a spherical mass M for a stationary timelike observer (with 4-velocity $u^\alpha = \frac{\partial}{\partial t} = (1, 0, 0, 0)^T$) distant from said mass $r \in (2M, \infty)$. Worldly observers (such as ourselves) are timelike observers, and our geodesic path is such that $g_{\alpha\beta}\frac{\mathrm{d}x^\alpha}{\mathrm{d}\lambda}\frac{\mathrm{d}x^\beta}{\mathrm{d}\lambda} < 0$. A null geodesic is the path of a null observer, an object traveling at $c = 1$ (in other words, a photon). Otherwise, a spacelike ($g_{\alpha\beta}\frac{\mathrm{d}x^\alpha}{\mathrm{d}\lambda}\frac{\mathrm{d}x^\beta}{\mathrm{d}\lambda} > 0$) observer suggests an object moving faster than c, a feat violating Einstein's postulates and causality. A spacelike object should instead be interpreted as an object that occupies multiple points in space at a particular time.

The coordinate singularity at $r = 2M$ appears in these particular coordinates. One finds such a singularity by evaluating the metric (1.4) at $r = 2M$ and seeing $g_{tt} \to 0$.

One also may interpret this coordinate singularity as due to there not being any stationary timelike observers within this $r = 2M$ region (as only null observers may be stationary at $r = 2M$ and spacelike observers may be stationary at $r < 2M$). A similar effect occurs on the z-axis as $g_{\phi\phi}|_{\theta=0,\pi} \to 0$, but this coordinate degeneracy at the poles is a well known issue when defining coordinates on a sphere. A clearer way of seeing the effects of the coordinate singularity is to consider radial null geodesic curves as demonstrated in Figure 1.1. Null geodesic curves can be solved for by evaluating $g_{\alpha\beta} \frac{\mathrm{d}x^\alpha}{\mathrm{d}\lambda} \frac{\mathrm{d}x^\beta}{\mathrm{d}\lambda} = 0$ where x^α is the curve's position vector and λ is some parameter along the curve. The divergence of the null geodesics in this coordinate chart at $r = 2M$ shows the timelike coordinate becoming ill-defined at this horizon (see Figure 1.1). The curves (red and blue) asymptotically approach $r = 2M$, diverging to $t \to \pm\infty$, denying the coordinates access to the black hole interior.

We further improve upon our understanding of this spacetime by finding the coordinate transformations to achieve the *compactified* Schwarzschild spacetime in the form of Penrose-Carter diagrams. Through double-null coordinates

$$u = t - r - 2M \ln \left| \frac{r}{2M} - 1 \right| \quad ; \quad v = t + r + 2M \ln \left| \frac{r}{2M} - 1 \right| \qquad (1.5)$$

the compactified coordinates are

$$U = \tan^{-1} \left(\pm e^{\frac{-u}{4M}} \right) \quad ; \quad V = \tan^{-1} \left(e^{\frac{v}{4M}} \right) \qquad (1.6)$$

This maps $u, v \in (-\infty, \infty)$ to $U, V \in (-\pi/2, \pi/2)$. When plotting it, such as in Figure 1.2, the orientation is such that null geodesics (photons, light rays) travel at $45°$ angles. Correspondingly, timelike observers strictly travel at an angle steeper than $45°$ or are otherwise spacelike observers. As such, all timelike geodesics will either

4
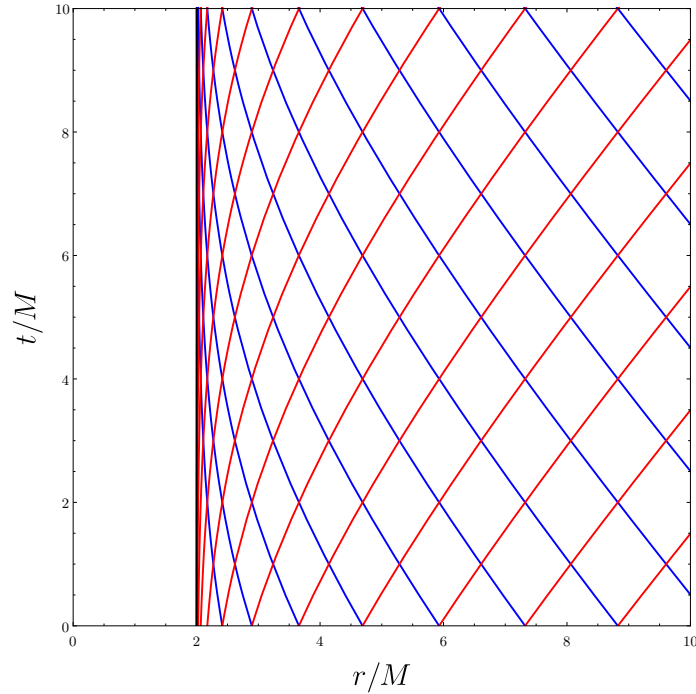
Figure 1.1: Null geodesics in the Schwarzschild spacetime in $\{t, r\}$ coordinates $r \in (2M, \infty)$. The blue curves are in-going null geodesics and the red curves are the out-going ones. Derivations of these curves can be found in Appendix A.1.

remain outside the black hole and tend toward future timelike infinity or encounter the spacetime singularity at $r = 0$. Refer to Table 1.1 for each point in the compactified spacetime.

A coordinate singularity is different from a spacetime singularity, the latter being a much more serious issue in the discontinuation of the manifold itself. This spacetime singularity can be found by evaluating the Kretschmann scalar (contraction of Riemann tensors), which comes out to be $R_{\alpha\beta\gamma\delta}R^{\alpha\beta\gamma\delta} = 48M^2/r^6$ for the Schwarzschild spacetime. This Kretschmann scalar is yet another curvature invariant, meaning that the singularity at $r = 0$ is a true spacetime singularity at the level of the manifold
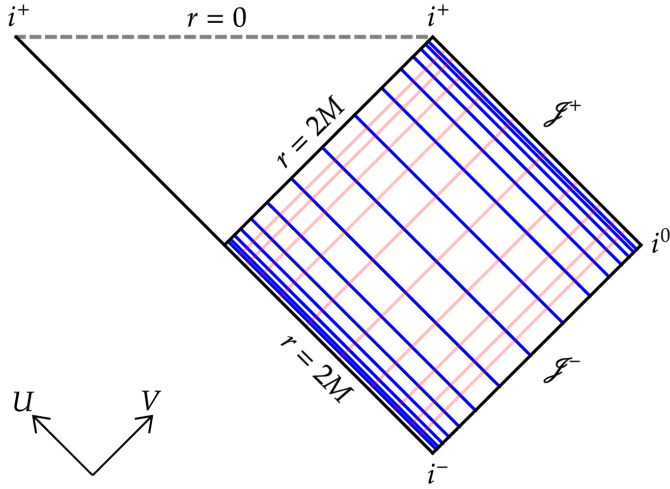
Figure 1.2: A Penrose-Carter diagram of the Schwarzschild spacetime. The blue and (low opacity) red lines are null geodesics in Schwarzschild coordinates, in particular, the ones plotted in Figure 1.1.

$\mathcal{M}$. The coordinate singularity at $r = 2M$ can be patched with several choices of coordinate transformations.

The set of 'horizon penetrating' coordinates we will focus on is the Painlevé–Gullstrand (PG) coordinates, which interprets the Schwarschild solution from the perspective of a free-falling observer starting from rest at infinity [7, pg. 168]. Such an observer's proper time $\tilde{t}$ would be defined as

$$\mathrm{d}\tilde{t} = \mathrm{d}t + \frac{\sqrt{2M/r}}{1 - 2M/r}\mathrm{d}r \tag{1.7}$$

giving rise to the Schwarzschild black hole in PG coordinates

$$\mathrm{d}s^2 = -\left(1 - \frac{2M}{r}\right)\mathrm{d}\tilde{t}^2 + 2\sqrt{2M/r}\ \mathrm{d}\tilde{t}\ \mathrm{d}r + \mathrm{d}r^2 + r^2\mathrm{d}\Omega^2\ . \tag{1.8}$$

Looking at null geodesics in these coordinates shows us the accessibility of the black hole interior as well as the inescapability past the $r = 2M$ horizon. In Figure

6

Label	Name	(U, V)	Definition
$\mathscr{I}^+$	Future null infinity	$U \in (-\pi/2, 0),\ V = \pi/2$	$v = \infty,\quad u$ finite
$\mathscr{I}^-$	Past null infinity	$V \in (0, \pi/2),\quad U = -\pi/2$	$u = -\infty, v$ finite
i^0	Spactial infinity	$(U, V) = (-\pi/2, \pi/2)$	$r = \infty,\quad t$ finite
i^+	Future timelike infinity	$(U, V) = (0, \pi/2);\ (\pi/2, 0)$	$t = \infty,\quad r$ finite
i^-	Past timelike infinity	$(U, V) = (-\pi/2, 0)$	$t = -\infty,\ r$ finite

Table 1.1: Dictionary of labels on the Penrose-Carter diagrams. Definitions align with the naming conventions in [7].

1.3, the in-going null geodesics pass through the now patched $r = 2M$ horizon and encounter the singularity. However, when we look at the out-going null geodesics, the curves within the $r = 2M$ horizon do not move radially outwards as one would expect, but instead seem to begin near the interior of the horizon and go into the $r = 0$ singularity. This is made clear with the Penrose-Carter diagram in Figure 1.4, which shows us that any null (or timelike) observer in $r \in (0, 2M)$ is doomed to eventually run into $r = 0$ with no hopes of escaping.

It is simple to find that this Schwarzschild radius matches the escape radius for an outward shot photon through the Newtonian calculation $v_e = \sqrt{2M/r}$ and setting the escape velocity $v_e = c = 1$. For a dense enough object that is radially smaller
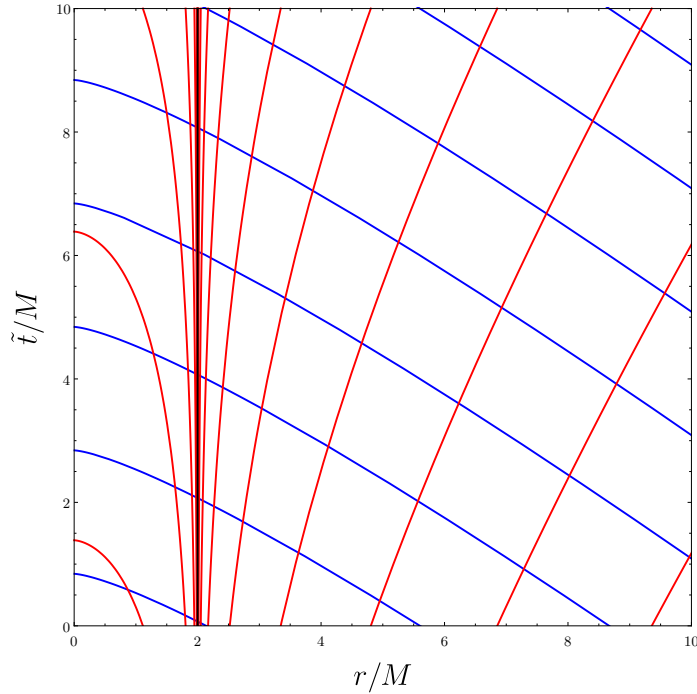
Figure 1.3: In-going null geodesics in the Schwarzschild spacetime in $\{\tilde{t}, r\}$ coordinates. Blue lines are ingoing geodesics from further away and red lines are outgoing ones. Derivations of these curves can be found in Appendix A.2.

than $r = 2M$, a black hole is formed with its boundary at $r = 2M$ popularly known as its *event horizon*. This nomenclature needs to be clarified, as an event horizon is a teleological surface, formally defined as the "boundary of the complement of the past-null cone of future null infinity" [8, 9]. The most obvious way to see the effects of such a surface is in either one of the Penrose-Carter diagrams (Figures 1.2 or 1.4), as one sees that all timelike observers within the event horizon strictly approach the $r = 0$ singularity and is thus causally isolated from the rest of the spacetime $r > 2M$. This means that one must understand the spacetime in its entirety ($t \in (-\infty, \infty)$) to classify a surface as an event horizon.
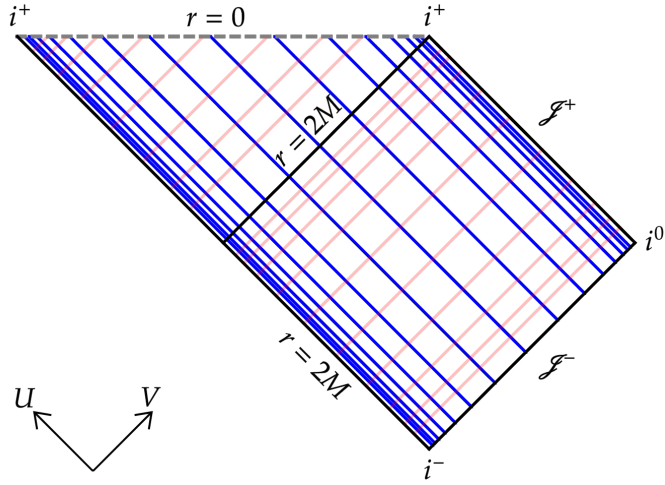
Figure 1.4: A Penrose-Carter diagram of the Schwarzschild spacetime. The blue and (low opacity) red lines are null geodesics in PG coordinates, in particular, the ones plotted in Figure 1.3.

Event horizons are not observable at any time slice ($t = $ constant) so it is instead preferable to consider *apparent horizons* [8, 9]. To interpret such an horizon, it is sufficient to look at the out-going null geodesics in Figures 1.3 and 1.4. Radially out-going null curves are trapped for $r \leq 2M$, the *trapped region* in this spacetime, the black hole. These terms will be defined more formally in the following paragraphs.

The apparent horizon is also taken to be the outer-most *marginally outer-trapped surface* (MOTS) by [8]. Introduced by Penrose for proving the singularity theorem [1], such surfaces are prime candidates to characterize the boundary of black holes. We now define what a MOTS is. Consider a smooth, closed 2-surface $\mathcal{S}$ with in- and out-going future-directed null normals $\ell^\alpha_{(-)}$ and $\ell^\alpha_{(+)}$ respectively. This surface is called a MOTS if its outward null expansion vanishes

$$\Theta_{(+)} = q^{AB} \hat{e}^\alpha_A \hat{e}^\beta_B \nabla_\alpha \ell^{(+)}_\beta = 0 \tag{1.9}$$

9

where q^{AB} is the inverse induced metric on $\mathcal{S}$: $q_{AB} = g_{\alpha\beta}\hat{e}^\alpha_A\hat{e}^\beta_B$; $\hat{e}^\alpha_A$ is the push-forward/pull-back operator $\hat{e}^\alpha_A = \frac{\partial x^\alpha}{\partial x^A}$ (partial derivatives between coordinates of the (3+1)-D geometry and the 2-D geometry), analogous to the Jacobian matrix); and ∇_α is the usual covariant derivative $\nabla_\alpha\ell_\beta = \frac{\partial \ell_\beta}{\partial x^\alpha} - \Gamma^\mu_{\alpha\beta}\ell_\mu$ for the Christoffel symbol $\Gamma^\mu_{\alpha\beta} = \frac{1}{2}g^{\mu\nu}\left(\frac{\partial g_{\beta\nu}}{\partial x^\alpha} + \frac{\partial g_{\alpha\nu}}{\partial x^\beta} - \frac{\partial g_{\alpha\beta}}{\partial x^\nu}\right)$.

The null vectors can be split into orthogonal unit timelike u and spacelike n parts such that:

$$\ell^\alpha_{(+)} = u^\alpha + n^\alpha \quad ; \quad u^\alpha u_\alpha = -1 \quad ; \quad n^\alpha n_\alpha = 1 \quad ; \quad u^\alpha n_\alpha = 0 \quad (1.10)$$

The timelike part u is interpreted as the vector normal to the constant time slice Σ and the spacelike part n is the normal to the MOTS itself living in the slicing (refer to Figure 1.5 for a diagram depicting this imagery). Both u and n are normals to $\mathcal{S}$
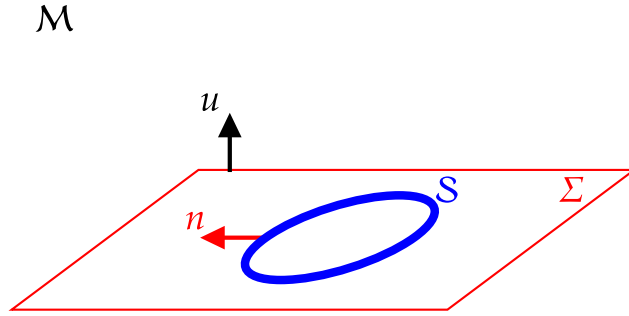
Figure 1.5: A diagram depicting a Lorentzian (3+1)-D manifold $\mathcal{M}$, the 3D spacelike time foliation Σ (characterized by the timelike normal u), and the 2D surface $\mathcal{S}$ (characterized by the spacelike normal n). The dimensions of the objects in the diagram are to be interpreted as stated in the caption.

and are constructed in such a way that $\ell^\alpha_{(+)} = u^\alpha + n^\alpha$ is null. The usefulness of this

formulation will become apparent in the demonstrative calculation we will do next, in calculating the expansions (Θ) of spherical surfaces in the Schwarzschild spacetime.

Starting with the Schwarzschild spacetime in PG coordinates (Eqn. (1.8)), constant $\tilde{t}$ slices ($\mathrm{d}\tilde{t} \to 0$) will leave an induced metric on Σ as

$$h_{ij}\mathrm{d}x^i\mathrm{d}x^j = \mathrm{d}r^2 + r^2\mathrm{d}\Omega^2 \tag{1.11}$$

The timelike (unit) normal to this slice is the one-form $u_\alpha \mathrm{d}x^\alpha = -\mathrm{d}\tilde{t}$, in vector form is $u^\alpha \frac{\partial}{\partial x^\alpha} = \frac{\partial}{\partial \tilde{t}} - \sqrt{2M/r}\frac{\partial}{\partial r}$. From the vector form, we see that u is future-oriented (toward positive $\tilde{t}$). Next, restricting to spherical surfaces (of radius r_0), we find the spacelike (unit) normal to be $n^\alpha \frac{\partial}{\partial x^\alpha} = \frac{\partial}{\partial r}$. The coordinates left on the surface $\mathcal{S}$ are θ and ϕ with an induced metric $q_{AB}\mathrm{d}x^A\mathrm{d}x^B = r_0{}^2 \left(\mathrm{d}\theta^2 + \sin^2\theta \mathrm{d}\phi^2\right)$–the geometry of a sphere with radius r_0. The two sets of coordinates $\{x^\alpha : \tilde{t}, r, \theta, \phi\}$ and $\{x^A : \theta, \phi\}$ allows us to show the push-forward/pull-back operator explicitly for this case: $\hat{e}^\alpha_A = \frac{\partial x^\alpha}{\partial x^A} = \delta^\alpha_A$. Grinding through the Einstein-convention contractions and covariant derivative, we arrive at the outward-null expansion $\Theta_{(+)}$ for our outward-null normal $\ell^{(+)}_\alpha = u_\alpha + n_\alpha$:

$$\Theta_{(+)} = \frac{2}{r_0}\left(1 - \sqrt{2M/r_0}\right) \tag{1.12}$$

The expansion vanishes at the expected $r_0 = 2M$ spherical horizon, and is our only spherical MOTS in the Schwarzschild spacetime. One can further analyze the Schwarzschild black hole with this expansion expression (Eqn. (1.12)): the expansion is negative for spheres $r_0 < 2M$ and positive for $r_0 > 2M$. The negative outward expansion characterizes an *outer-trapped* surface. If one expands their surface along their (outward) null vector $\ell_{(+)}$ in the $r < 2M$ region, the surface decreases in size

towards the $r = 0$ singularity–as Figures 1.3 & 1.4 show the tendencies of null curves within the black hole.

Similarly, one looks at the inward null expansion $\Theta_{(-)}$ of the same surface $\mathcal{S}$ but with null normals that are oriented 'inward' (and are still future-oriented): $\ell^\alpha_{(-)} = \frac{1}{2}(u^\alpha - n^\alpha)$. The factor of 1/2 is such that the normalization $\ell^\alpha_{(+)} \ell^{(-)}_\alpha = -1$ holds. The surface $\mathcal{S}$ is then classified as variants of trapped or untrapped surfaces, laid out in Table 1.2. A definition of the trapped region and its boundary, the apparent

Name of closed surface $\mathcal{S}$	$\Theta_{(+)}$	$\Theta_{(-)}$
untrapped	> 0	< 0
trapped	< 0	< 0
outer-trapped	< 0	No restriction
marginally outer-trapped	$= 0$	No restriction

Table 1.2: Dictionary of names for surfaces with corresponding expansions. This convention aligns with [8].

horizon, can be laid out following [8]. On a time-slice Σ, a trapped region is the set of all points $q \in \Sigma$ such that there is a trapped surface S in Σ through q. The apparent horizon is defined to be the boundary of this trapped region.

For many static and stationary black hole solutions (where the metric $g_{\alpha\beta}$ is independent of time) the event horizon and apparent horizon coincide (along with

several other geometrical horizons such as the Cauchy and Killing horizons). The difference between the event and apparent horizons become obvious when one looks at dynamic solutions, although [8] shows that the event horizon is necessarily outside or coinciding with the apparent horizon.

One dynamic scenario that is of interest is that of black hole mergers. With engineering advancements allowing for laser interferometry precise enough to discern gravitational waves, the LIGO-Virgo collaboration were the first to observe this phenomenon [10]. This emerging frontier of observational astronomy yearns for a fuller understanding of the black hole merger process. The merger of a binary black hole system is an open-ended problem that dates back ∼50 years. The understanding of the merger process is encapsulated in Figure 1.6. Many refer to the figure as the "pair of pants" diagram, as the progression of the event horizon seems to outline a pair of pants. The merger of two black holes demonstrate some key features of dynamic black hole systems, such as the distinction of event and apparent horizons and the creation then bifurcation of the enveloping apparent horizon. Creation-bifurcation events of apparent horizons such as these are not uncommon, the dynamical case of a collapsing black hole exhibits a similar phenomenon.

Figure 1.6 is to be read from bottom up as the black hole merger evolves in time. Near the ankles of the pants, the two black holes are still far apart, with the separation of each event and apparent horizons a consequence of their influence on each other. The event horizons eventually join, but the apparent horizons continue to persist separately. Once the two black holes are sufficiently close, a creation-bifurcation event occurs with two enveloping apparent horizons. The outer enveloping horizon will become the resultant black hole's apparent horizon, which will asymptote
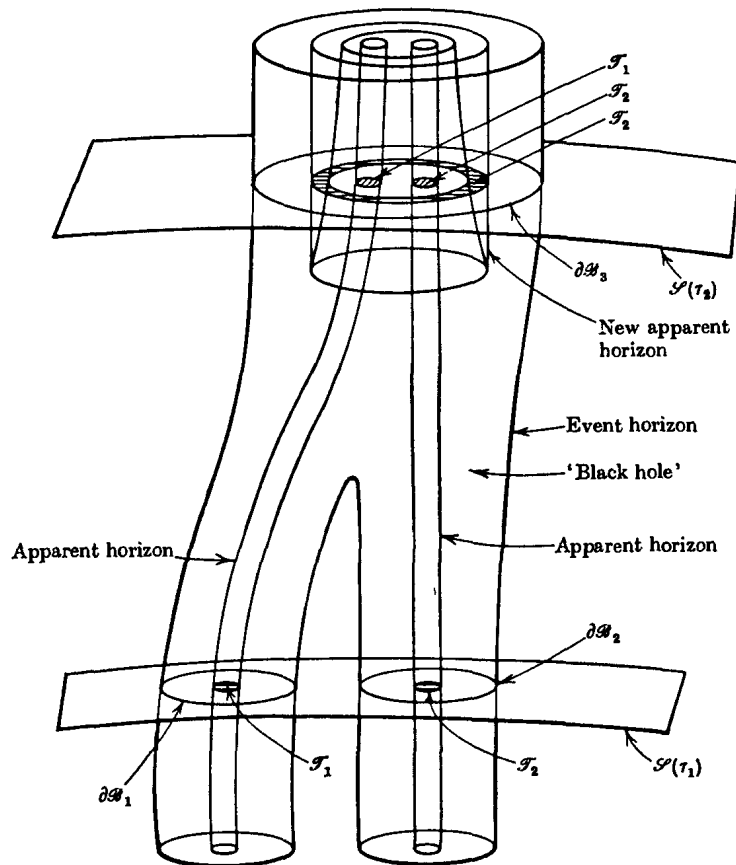
Figure 1.6: The collision and merger of two black holes. Time flows in the upward direction. The plot depicts event and apparent horizons as the merger process follows through. This figure is taken from [8, pg. 322 Figure 60].

towards the resultant event horizon as the merger approaches a steady state. The missing parts of this merger picture rests in the original two apparent horizons and the inner enveloping horizon. These three structures are not found in the interior of the Schwarzschild black hole, the solution which the merger approaches, and thus they must undergo some annihilation process later along the evolution.

As black holes are described by the curvature of the spacetime around them, the union of two black holes such as this is a very non-linear process (since the Einstein

equations are a set of non-linear equations). Therefore, it is difficult to analyze the evolution of the three horizons. Turning to numerical simulations, more issues arise with the methods to find apparent horizons. With complications hindering the understanding of these three structures and their fate, binary black hole mergers have not been fully understood.

The rest of this thesis explores the resolution to this problem as well as the emergence of an exotic phenomenon as follows. Chapter 2 considers the limitations in our understandings of the black hole merger and recent developments that have allowed us to resolve it better. This part includes the appearance of self-intersecting MOTS and a particular discovery about the stability of these self-intersecting MOTS. Chapter 3 finds similarly self-intersecting MOTS in the case of the Schwarzschild black hole when one considers axisymmetric surfaces. The methodology behind the finding of these MOTS will be introduced in this part as well as the automation developed to be used in chapter 4. This algorithm and the rest of the thesis is part of the original work of this thesis. Chapter 4 presents findings from the search for self-intersecting MOTS in two non-vacuum black hole solutions. One of these spacetimes–the Reissner-Nordström spacetime–requires further generalization of the Painlevé-Gullstrand coordinate transformation in order to fully probe into the charged black hole. The other–the 4-dimensional-limit Gauss-Bonnet black hole–further fuels the stability observation in chapter 3. Finally, chapter 5 provides a discussion on the results, an outlook of the research, and concluding remarks.

Chapter 2

Background

In this chapter, we consider more recent developments that form important background to the rest of the thesis. In particular, we first consider the evolution of MOTSs during black hole mergers and then consider the *stability operator* which provides further geometric information about a MOTS.

2.1 Black hole mergers

The issue to be addressed is the evolution of the three main horizons in the binary black hole merger process: the original two horizons plus the common horizon that forms post-merger. Due to the non-linear nature of the merger, analytical models of the merger are not possible outside the scope of perturbative and asymptotic limits near the beginning or end—a problem dating back to 1964 in the works of Hahn & Lindquist [11]. Therefore, one turns to numerical simulations to evolve the two-body problem [12]. Although there have been very significant recent numerical developments [13], there was some success of such numerically evolving merging black

hole horizons as early as 1995 [14]. With leaps in computational power and methods, a numerical resolution to the three horizons draws near.

Traditional numerical methods in finding apparent horizons worked by using a reference point and assumed a straight line of sight from that point to any point on the MOTS [15]. This popular method is since been incorporated into the Einstein toolkit as `AHFinderDirect` [16]. However, this method is heavily restricted to only find 'star-shaped' (or round)-shaped MOTS. During a binary black hole merger, the interior enveloping common horizon gradually tends towards wrapping the two original apparent horizons, and as such can no longer be tracked as it deviates away from being star-shaped. Figure 2.1 demonstrates this failure, as the inner common horizon distorts beyond the scope of the MOTS finder.
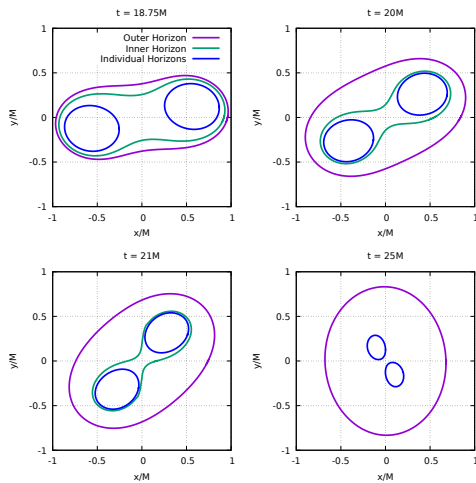

Figure 2.1: Plots depicting the horizons in question during a numerically simulated black hole merger at increasing time t. This evolution of panels demonstrates the inner enveloping horizon deviating from being round enough to be found using `AHFinderDirect`. The plots are taken from [17, Figure 3].

A new MOTS-finding method was proposed in 2018 that instead uses a surface as the reference rather than a single point [18]. Figure 2.2 shows this new method compared to the old method.
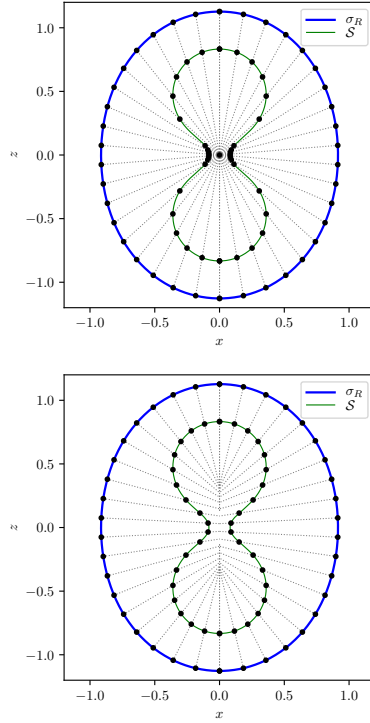
Figure 2.2: Plots depicting how the two horizon finders search for a barely star-shaped MOTS $\mathcal{S}$. The first panel is the method used in `AHFinderDirect` [15]. The second panel demonstrates the reference surface σ_R used instead in [18]. The plots are taken from [18, Figure 2].

In this case, the `AHFinderDirect` method using the origin as its reference point struggles to resolve the MOTS near the y-axis since $\mathcal{S}$ has a high curvature there. This is seen with the high concentration of black dots on $\mathcal{S}$. If $\mathcal{S}$ were to distort away from from its star shape any further, the black dots near the $y = 0$ axis would start

disappearing – meaning that chunks of the $\mathcal{S}$ would be unattainable by the finder. The newer method uses the surface σ_R as its reference surface and the black dots are more evenly spread across $\mathcal{S}$. With this new method, non-star-shaped MOTS may be found. With the star-shape restriction lifted, the unanswered question of how the three horizons evolve during a black hole merger may be probed further, as done so in [19, 20]. The results can be summarized in Figure 2.3.

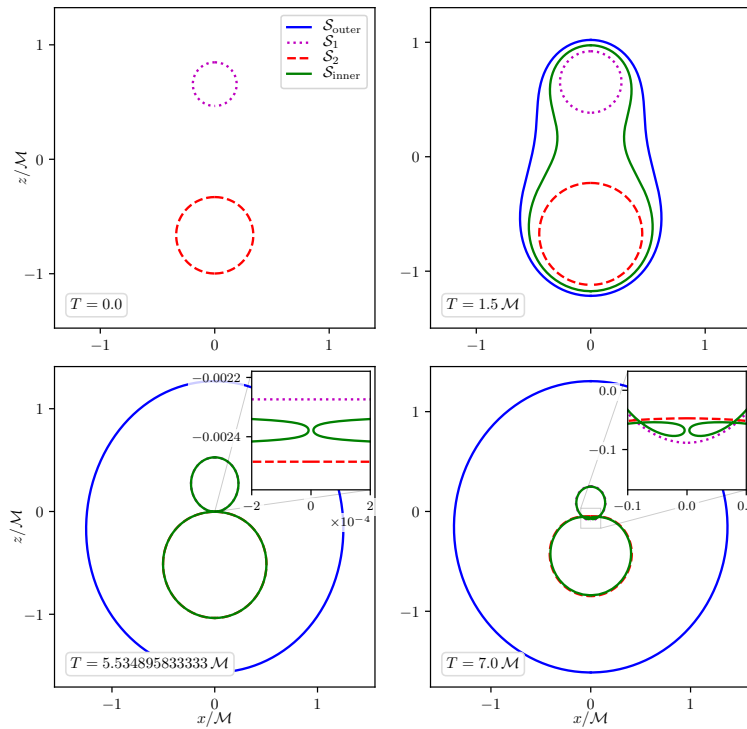Figure 2.3: Plots depicting a numerically simulated black hole merger (head-on collision, no angular momentum) for increasing time T. The two original black holes' horizons are $\mathcal{S}_1$ and $\mathcal{S}_2$, the common enveloping horizons are $\mathcal{S}_{\text{outer}}$ and $\mathcal{S}_{\text{inner}}$. The plots are taken from [20, Figure 1].

The top two panels recreate what is already known–the two original apparent

horizons $\mathcal{S}_1$ and $\mathcal{S}_2$ approaching each other and then common enveloping horizons $\mathcal{S}_{\text{outer}}$ and $\mathcal{S}_{\text{inner}}$ forming in a bifurcation event. The bottom-left panel shows that the inner-common horizon $\mathcal{S}_{\text{inner}}$ tends to a cusp until it coincides with the two apparent horizons when they touch. Once the two apparent horizons intersect each other, a self-intersection is found of $\mathcal{S}_{\text{inner}}$ in the overlapping area. Although it was initially unclear whether the claimed $\mathcal{S}_{\text{inner}}$ is the same surface from its enveloping shape to the coinciding cusp shape to the self-intersection shape, evidence supporting this claim is found in [21, 22].

This new MOTS-finding method has already shown to be powerful in this deeper probing of the merger process and the discovery of the self-intersecting MOTS. The limitation then lies in the choice of the reference surface σ_R, as one would have to guess a rough shape of the MOTS in order to find it.

In practice, the MOTS-finding method requires a sufficiently accurate reference surface. The MOTS from the previous time-step in black hole merger simulations is typically used as this reference surface. This method works well for tracking a known MOTS, but requires a good guess to find new ones or if the MOTS passes through singular surface configurations. In later chapters of this thesis, MOTSs are found in static spacetimes that are used as reference surfaces in black hole merger simulations.

A more systematic approach to finding MOTS can be attained by considering solutions to Eqn. (1.9). As demonstrated in the introduction, an exact solution could be found for simple spherical MOTS. The two numerical methods mentioned (the method used in [19, 20] and numerically integrating Eqn. (1.9)) are generic, accounting for MOTS of any shape. If one considers head-on collision binary black hole mergers, an axial symmetry constraint may be imposed, turning Eqn. (1.9) from what would

be a partial differential equation (for the generic case) into an ordinary differential equation (for axisymmetrical MOTS). This ultimately turns into a boundary-value problem (BVP) in order to preserve the smoothness condition of the MOTS. Among the numerical techniques to solve ODE-BVPs, the versatile shooting method is the method of choice [23]. This ODE-BVP and the application of the shooting method to numerically solving (1.9) will be elaborated upon in Chapter 3. Through this systematic MOTS-finding, many more self-intersecting MOTS were found during the critical moments of the binary black hole merger process.

Combined efforts give a clearer picture [21, 22], one that hints at a countless number of self-intersecting MOTS that contribute to a creation-annihilation waltz in the binary black hole process.
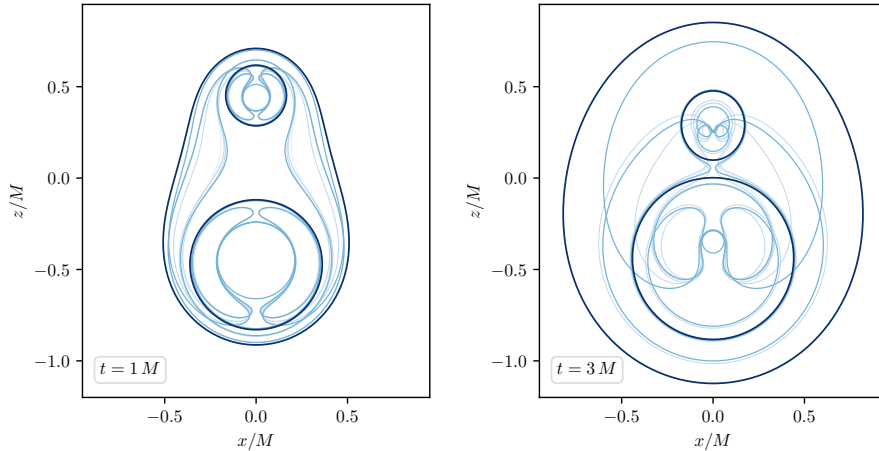
Figure 2.4: Figures of cross-sections of several MOTS found in two time foliations during the black hole merger process. The opacity and thickness of the MOTS depicted denote the number of negative eigenvalues of the MOTS' stability operator spectrum (introduced later on). Figures are taken from [22, Figure 16].
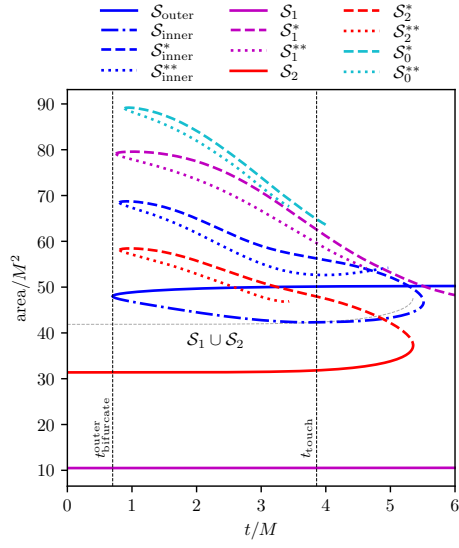
Figure 2.5: A plot of the areas of several MOTS during the binary black hole merger along time t. Plot is taken from [22, Figure 3].
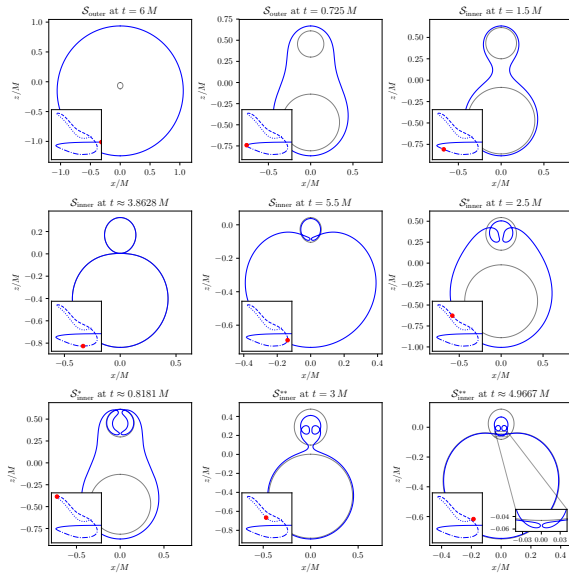
Figure 2.6: Plots of the MOTS involved in the annihilation of the inner common enveloping horizon and its siblings. Plots are taken from [22, Figure 4].

2.2 Geometry of MOTS: Stability Operator

Further information about a MOTS can be extracted from the *MOTS stability operator* L_Σ [21]:

$$L_\Sigma \psi := \delta_{\psi n^\alpha} \Theta_{(+)} \ . \tag{2.1}$$

The stability operator is defined to be the rate of change of the outward null expansion if $\mathcal{S}$ is deformed in the direction of the space-like vector $\nu = \psi n$, where $\psi = \psi(s)$ is an arbitrary deformation function. This deformation can be rewritten as [24–26]:

$$L_\Sigma \psi = -\Delta_{\mathcal{S}} \psi + \left(\frac{1}{2} \mathcal{R}_{\mathcal{S}} - 2|\sigma_+|^2 - 2G_{++} - G_{+-} \right) \psi \ , \tag{2.2}$$

where $\Delta_{\mathcal{S}} \psi = \tilde{\nabla}^A \tilde{\nabla}_A \psi$ is the Laplacian operator on the MOTS, $\mathcal{R}_{\mathcal{S}}$ the Ricci scalar of the MOTS, $|\sigma_+|^2 = \sigma_+^{AB} \sigma_{AB}^+$ is the square of the null shear $\sigma_{AB}^+ = \nabla_A \ell_B - \frac{1}{2}\Theta_{(+)} q_{AB}$, and the $G_{++} = G_{\alpha\beta} \ell_{(+)}^\alpha \ell_{(+)}^\alpha$ and $G_{+-} = G_{\alpha\beta} \ell_{(+)}^\alpha \ell_{(-)}^\alpha$ are the contraction of the Einstein tensor with respective null normals of $\mathcal{S}$. If the deformation function ψ is either everywhere positive or negative [25], then one deforms the surface $\mathcal{S}$ always along the same orientated direction during the variation (either entirely outwards or inwards).

A few things can be gleaned from the stability operator by analysis of its discrete eigenvalue spectrum. In non-rotating spacetimes, L_Σ is self-adjoint and so the eigenvalue spectrum is real, hence discussion of the eigenvalue spectrum in this project is assumed to be always real. This eigenvalue spectrum of L_Σ provides further information about MOTS evolution, as shown in Figure 2.7. We now discuss the characteristics of a MOTS encoded in the eigenvalue spectrum. The always real [25] principal eigenvalue λ_0 of L_Σ by itself determines whether the MOTS may be understood as an apparent horizon. If a MOTS exhibits a 'barrier' property[1], as is characteristic of an

---

[1]this "barrier" property is called "local outermost" from [25], denoting the outermost MOTS.

apparent horizon, then one expects $\delta_v \Theta_{(+)} > 0$ – that is, as you deform the surface outward, the expansion $\Theta_{(+)}$ increases and so $\Theta_{(+)} > 0$ (as one expects outside the trapped region of the black hole). From this observation, $\lambda_0 > 0$, which classifies the 'barrier' MOTS as *strictly stable* [25]. The MOTS is otherwise classified as *unstable* if $\lambda_0 < 0$ and *marginally stable* if $\lambda_0 = 0$.

If $\lambda_0 = 0$, then there is a corresponding eigenfunction ψ_0 that satisfies $\delta_{\psi_0 n} \Theta_{(+)} = 0$. This suggests a situation where there are multiple coinciding MOTSs. Such instances include creation-bifurcation and annihilation cases, resulting in a vanishing eigenvalue at the moment of bifurcation/annihilation. In these cases, the eigenvalue spectrum carries a zero eigenvalue (that is not necessarily the principal eigenvalue). This is observed in the eigenvalue spectrum in the binary black hole merger, as shown in the plots of Figure 2.7. Though not directly relevant to this project, there is an observed relationship between the number of negative eigenvalues (for $m = 0$, defined shortly later). and number of self-intersections:

$$\# \text{ self-intersections} = \lfloor \frac{\# \text{ negative } \lambda\text{'s}}{2} \rfloor \ .$$

Every pair of negative eigenvalues was found to correspond to one self-intersection.

This discrete spectrum of the stability operator may be numerically approximated. First, the deformation function $\psi(s, \phi)$ can be separated (thanks to the rotational symmetry about the z-axis) as

$$\psi(s, \phi) = \sum_{m=-\infty}^{\infty} \psi_{lm}(s) \exp(im\phi) \ , \tag{2.3}$$

after which the eigenvalue problem $L_\Sigma \psi = \lambda \psi$ reduces to

$$(L_\Sigma + m^2 q^{\phi\phi})\psi_{lm} = \lambda \psi_{lm} \ , \tag{2.4}$$

24
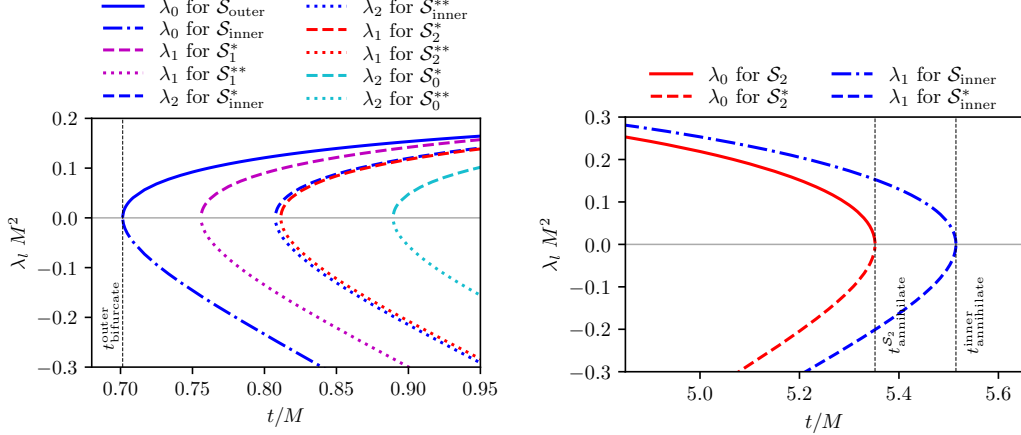
Figure 2.7: Plots of particular eigenvalues λ of the stability operator on particular MOTSs $\mathcal{S}$ near times t at which said MOTS exhibit bifurcation and annihilation events during a binary BH merger. Figures are taken from [22, Figure 14 and 15].

where m is the second quantum number that we will set to zero $m = 0$ in axisymmetry. The $m \neq 0$ cases may be associated to the angular deformations along the ϕ direction and are expected to give complex eigenvalues with nonzero imaginary components.

To numerically solve this eigenvalue problem, we employ a pseudo-spectral method [27, 28]. Consider a MOTS $\mathcal{S}(s, \phi)$ that spans the parameterization $s \in [0, s_{\max}]$. We expand the eigenfunction $\psi_m(s)$ in a Chebyshev series:

$$\psi_{m=0}(s) = \sum_{k=0}^{N} a_k \cos\left(\frac{k\pi s_i}{s_{\max}}\right) , \tag{2.5}$$

where s_i are $N + 1$ discretized points along $s \in [0, s_{\max}]$. A matrix approximation is then constructed from these discretized functions where $L_{ik} = (L_\Sigma \phi_k)(s_i)$ and $\Phi_{ik} = \phi_k(s_i)$:

$$L_\Sigma \psi = \lambda \psi \rightarrow L_{ik} a_k = \lambda \Phi_{ik} a_k . \tag{2.6}$$

The eigenvalues λ are then simply eigenvalues of the matrix $\mathbf{M = \Phi^{-1}L}$, which we use

built-in functions in Mathematica to compute. The indices i and k need to run over $N+1$ values as the matrices need to be square. This means that the number of points along the MOTS sampled s_i corresponds to the number of Chebyshev polynomials to be computed. Picking on the order of $N = 100$ is sufficient for good convergence of the eigenvalue spectrum, though larger N is needed for convergence in some cases.

In numerical simulations it has been observed that, a vanishing principal eigenvalue corresponds to apparent horizons at the moment of its annihilation with another surface, or some otherwise non-smooth evolution event [24, 25]. What we will find are examples of annihilation events corresponding to non-principal, $m = 0$, eigenvalues in the case of self-intersecting MOTSs. It is speculated that vanishing $m \neq 0$ eigenvalues are associated with bifurcation events of non-axisymmetric MOTSs but this is outside the scope of this thesis.

Chapter 3

Self-intersecting MOTS in the Schwarzschild spacetime

The extensive investigation of self-intersecting MOTSs in the numerically obtained binary black hole merger spacetimes were limited in their MOTS-finder methods and numerical precision. Therefore, finding accurate late-stage merger spacetimes is no easy feat, requiring the computational power of computer clusters [29, 30]. On top of this, the MOTS-finding method introduced in [18] is restricted by the initial surface fed to the finder. Further evidence for the existence of self-intersecting MOTS like those found during black hole mergers came from an unexpected source: they were also found in static, exact spacetimes.

This can be achieved by considering the simplest static black hole solution known – the Schwarzschild solution. The calculation for finding the $r = 2M$ spherical MOTS had already been shown in the Introduction. However, if one extends the constraints to axi-symmetric MOTSs rather than spherical ones, the requirement that the null

expansion vanishes corresponds to a coupled pair of ordinary differential equations. These can be numerically solved to find the self-intersecting MOTSs.

Recall the Schwarzschild black hole in Painlevé–Gullstrand (PG) coordinates:

$$g_{\alpha\beta}\mathrm{d}x^\alpha\mathrm{d}x^\beta = -\left(1 - \frac{2M}{r}\right)\mathrm{d}\tilde{t}^2 + 2\sqrt{2M/r}\,\mathrm{d}\tilde{t}\,\mathrm{d}r + \mathrm{d}r^2 + r^2\mathrm{d}\Omega^2 \ ,$$

where constant $\tilde{t}$ slices exhibit an intrinsically flat geometry $h_{ab}\mathrm{d}x^a\mathrm{d}x^b = \mathrm{d}r^2 + r^2\mathrm{d}\Omega^2$. Since we only consider axi-symmetrical MOTS (invariant about rotation in the ϕ direction), it is useful to parameterize the 2-dimensional MOTS with $r = R(s)$ and $\theta = \Theta(s)$, giving the parameterized 2-dimensional surface the geometry q_{AB}:

$$q_{AB}\mathrm{d}x^A\mathrm{d}x^B = (\dot{R}^2 + R^2\dot{\Theta}^2)\mathrm{d}s^2 + R^2\sin^2\Theta\mathrm{d}\phi^2 \ , \tag{3.1}$$

with dots symbolizing derivatives with respect to the parameter coordinate s. In the induced metric (3.1), one sees the inherent axis-symmetry as q_{AB} is independent of ϕ. This means we can take a constant $\phi \in [0,\ 2\pi)$ slice leaving a line element that reads $(\dot{R}^2 + R^2\dot{\Theta}^2)\mathrm{d}s^2$. We may impose an 'arc-length condition' to equate the parameter s to be the arc-length of the one-dimensional curve found when one performs a constant ϕ slicing of such a MOTS (as depicted in Figure 3.2):

$$\dot{R}^2 + R^2\dot{\Theta}^2 = 1 \ . \tag{3.2}$$

With our coordinates defined on our 2-dimensional surface, this allows us to construct the push-forward/pull-pack operator between the four and two dimensional geometries. With $x^\alpha = \{\ \tilde{t},\ r,\ \theta,\ \phi\}$ and $x^A = \{\ s,\ \phi\}$:

$$e_A{}^\alpha = \frac{\partial x^\alpha}{\partial x^A} = \begin{pmatrix} 0 & \dot{R} & \dot{\Theta} & 0 \\ 0 & 0 & 0 & 1 \end{pmatrix} . \tag{3.3}$$

28

The unit spacelike normal n can then be constructed satisfying

$$n^\alpha n_\alpha = 1 \quad ; \quad n^\alpha u_\alpha = 0 \quad ; \quad n_\alpha e_A^\alpha = 0 \ .$$

This system of conditions can be solved to obtain

$$n^\alpha \left(\frac{\partial}{\partial x^\alpha} \right) = R\dot{\Theta} \left(\frac{\partial}{\partial r} \right) - \frac{\dot{R}}{R} \left(\frac{\partial}{\partial \theta} \right) \ . \tag{3.4}$$

The outward null expansion then works out to be

$$\Theta_{(+)} = -\sqrt{\frac{M}{2R^3}} \left(1 + 3R^2\dot{\Theta}^2 \right) + R \left(\dot{R}\ddot{\Theta} - \dot{\Theta}\ddot{R} \right) + \dot{\Theta} \left(3\dot{R}^2 + 2R^2\dot{\Theta}^2 \right) - \frac{\dot{R}\cot\Theta}{R} \ . \tag{3.5}$$

Solutions to $\Theta_{(+)} = 0$ are MOTS. The vanishing outward null expansion $\Theta_{(+)} = 0$ is solved exactly in the spherical case $R = 2M$, $\dot{R} = 0$, $\ddot{R} = 0$ (with $\dot{\Theta}^2 = (1 - \dot{R}^2)/R^2$), but is otherwise a system of non trivial coupled second-order ordinary differential equation (the system being equations (3.2) and (3.5)).

Numerically finding solutions to the vanishing expansion is possible without (3.2) as shown in [31] and evident in Figure 3.1. The method implemented is to create two equations out of $\Theta_{(+)} = 0$ by setting the parameter as either coordinates $s \to r$ or $s \to \theta$. This creates two differential equations–one a second-order ODE for $R(\theta)$ the other for $\Theta(r)$, then it is possible to numerically integrate for $R(\theta)$ and $\Theta(r)$. This process was quite involved–as many numerical singularities would be encountered requiring frequent switching between the equations for $R(\theta)$ and $\Theta(r)$. Once the solutions were stitched together, the self-intersecting MOTSs within the Schwarzschild black hole was found.

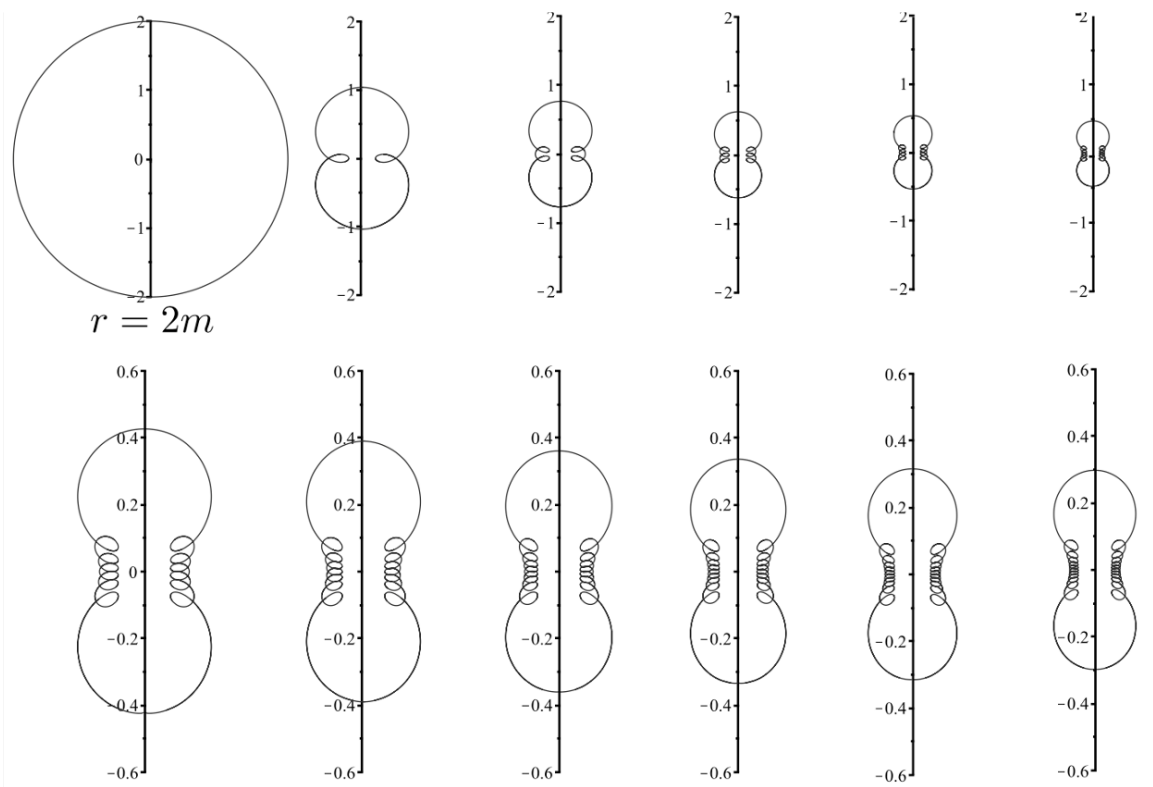Figure 3.1: Plots of the 12 outer-most axis-symmetric MOTSs. The vertical axis shown is the z-axis with $\rho = \sqrt{x^2 + y^2}$ along the horizontal, both in unit of the black hole's mass parameter. Curves shown are cross-sections of the MOTSs, on the half-planes $\phi = \text{constant}$ and $\phi = \text{constant} + \pi$. Interpretation of these figures can be found in Figure 3.2. Figures were provided by authors of [31].
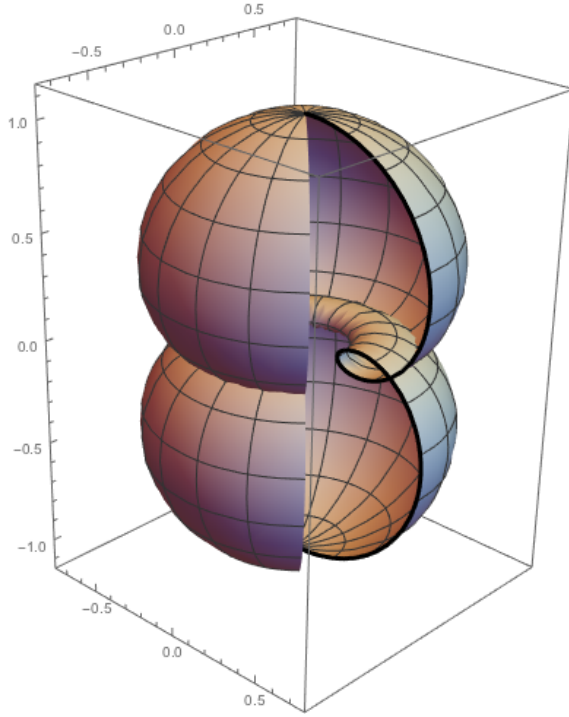
Figure 3.2: A three-dimensional rendition of the once-self-intersecting MOTS for a constant time slice. A bolded black line has been drawn to highlight the 1-dimensional curve plotted for a $\phi = \text{constant} = 0$ slice. Axes are usual Cartesian coordinates in units of the black hole's mass parameter.

The types of equations we will be numerically integrating in this thesis will use the arc-length parameterization (3.2). By differentiating (3.2), one encounters a system of coupled ODE's that is more easily (numerically) integrated:

$$
\begin{aligned}
\ddot{R} &= \tfrac{1}{2}\dot{\Theta}\left[-2\cot\Theta\,\dot{R} + 4R\dot{\Theta} + \left(-4 + 3\dot{R}^2\right)\sqrt{2M/R}\right] \\
\ddot{\Theta} &= \frac{\dot{R}}{2R^2}\left[2\cot\Theta\,\dot{R} - 6R\dot{\Theta} + \left(1 + 3R^2\dot{\Theta}^2\right)\sqrt{2M/R}\right] \ .
\end{aligned}
\tag{3.6}
$$

A standard numerical integration package is used to handle this–namely, Mathematica's `NDSolve[]` function is sufficient to find solutions to these equations.

31

Surfaces found from the equations in (3.6) do not necessarily close, meaning the 'closed' property of a MOTS is not guaranteed [31]. Such surfaces are categorized as *marginally outer-trapped open surfaces* (MOTOS), and the special cases of closure gives MOTS. Figure 3.3 The search for a MOTS then becomes a boundary-valued problem (BVP) for closed surfaces found out of (3.6).
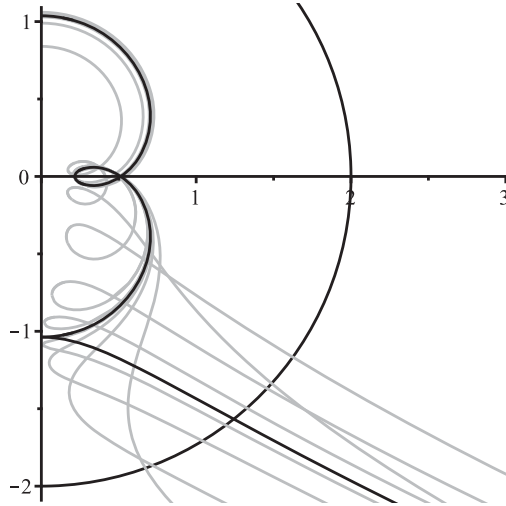
Figure 3.3: Plots of several MOTOS (in gray) and the two outer-most MOTS (in black) of the Schwarzschild spacetime in PG coordinates. The once-intersecting MOTS has a tail due to numerical inadequacies. Axes are the z-axis and $\rho = \sqrt{x^2 + y^2}$ in units of the black hole mass parameter.

By visual inspection of Figure 3.3, there is a singular repulsion characteristic at the z-axis. The 'tail' of the solid black self-intersecting MOTS shows this repulsion, as seen when the numerical result attempts to approach the z-axis perpendicularly and its imperfections causes the curve to diverge sharply. This can more easily real-ized if the MOT(O)S equations were considered in cylindrical spacetime coordinates

$\{\tilde{t}, \rho, z, \phi\}$ with similar parameterization $\rho = P(s)$, $z = Z(s)$ and $\dot{P}^2 + \dot{Z}^2 = 1$, rather than the current spherical coordinates $\{\tilde{t}, r, \theta, \phi\}$ (the two coordinates are related by $\tan \theta = \rho/z$ and $r^2 = \rho^2 + z^2$).

$$
\begin{aligned}
\ddot{P} &= \frac{\dot{Z}^2}{P} + \sqrt{\frac{M}{2(P^2 + Z^2)^{7/2}}} \left[\dot{P}^2(P^2 + 4Z^2) + \dot{Z}^2(4P^2 + Z^2) - 6PZ\dot{P}\dot{Z} \right] \\
\ddot{Z} &= -\frac{\dot{P}\dot{Z}}{P} - \sqrt{\frac{M}{2(P^2 + Z^2)^{7/2}}} \left[\dot{P}^2(P^2 + 4Z^2) + \dot{Z}^2(4P^2 + Z^2) - 6PZ\dot{P}\dot{Z} \right] .
\end{aligned}
\tag{3.7}
$$

In these coordinates, the first term of the equation for $\ddot{P}(s)$ shows the repulsive nature of the z-axis ($\ddot{P} \to \infty$ as $P \to 0$).

The shooting method is implemented–where initial conditions are given at one boundary, numerically propagated by evolution through the differential equations, and analyzed at the other boundary. Closed and smooth axis-symmetrical surfaces would exhibit perpendicularity with its axis of symmetry, hence the initial conditions desired for the Schwarzschild black hole in PG coordinates:

$$
\begin{aligned}
P(0) &= 0 \quad ; \quad \dot{P}(0) = 1 \\
Z(0) &= \pm z_0 \quad ; \quad \dot{Z}(0) = 0 .
\end{aligned}
\tag{3.8}
$$

The choice of $Z(0) = \pm z_0$ initiates the integration either above or below the x-y plane, respectively. In this manuscript, we initiate MOT(O)S constant slicing curves from the positive z-axis $Z(0) = z_0 > 0$. As evident by (3.7), the ODEs are singular at the axis of rotational symmetry ($P = 0$). Instead, leading orders of the initial conditions can be found, as the limits of each term towards the axis exists as $s \to 0$:

$$
\begin{aligned}
P(s) &= P(0) + \dot{P}(0)\, s + \frac{1}{2!}\ddot{P}(0)\, s^2 + \frac{1}{3!}P^{(3)}(0)\, s^3 + \frac{1}{4!}P^{(4)}(0)\, s^4 + \mathcal{O}(s^5) \\
Z(s) &= Z(0) + \dot{Z}(0)\, s + \frac{1}{2!}\ddot{Z}(0)\, s^2 + \frac{1}{3!}Z^{(3)}(0)\, s^3 + \frac{1}{4!}Z^{(4)}(0)\, s^4 + \mathcal{O}(s^5) .
\end{aligned}
\tag{3.9}
$$

The four leading terms are calculated to be

$$P(0) = 0 \quad ; \quad \dot{P}(0) = 1 \quad ; \quad \ddot{P}(0) = \lim_{s \to 0} \ddot{P}(s) = 0 \quad ; \quad P^{(3)}(0) = -\frac{2M}{z_0^{\ 3}}$$

$$Z(0) = z_0 \quad ; \quad \dot{Z}(0) = 0 \quad ; \quad \ddot{Z}(0) = -\frac{\sqrt{2M}}{z_0^{\ 3/2}} \quad ; \quad Z^{(3)}(0) = 0 \qquad (3.10)$$

$$P^{(4)}(0) = 0 \quad ; \quad Z^{(4)}(0) = \frac{\sqrt{M}\left(-9\sqrt{Mz_0} + 5\sqrt{2}M + 3\sqrt{2}\,z_0\right)}{z_0^{\ 9/2}} \ .$$

Evolving the initial conditions (outlined in equations (3.9) and (3.10)) using the MOT(O)S equations (3.7), curves displayed in Figure 3.3 are found and plotted. The black bolded curve signifies a surface that is implied to close. One may hand-tune initial z_0 values in the search for closed MOTS in the sea of infinite MOTOS. This search is sure to terminate, as a z_0 value too small will show MOTOS with two-self intersections and z_0 values too large will show MOTOS with just the one self-intersection (note the characteristic of the gray MOTOS curves adjacent to the black MOTS in Figure 3.3). The search for MOTSs may then be reduced to an optimization problem.

The observation that MOTSs are symmetric across the x-y plane allows for an automation of this MOTS-finding process. Asserting this symmetry allows for the evaluation of the distance from the z-axis at the location which one expects the MOTS to close. Namely, we get the curve parameter $s = s_0$ at which $Z(s_0) = -z_0$, and consider the radial distance from the axis $P(s_0)$. This is visualized in Figure 3.4a. This $P(s_0)$ value is an implicit function of the initial condition, particularly the $Z(0) = z_0$ value of which the curve is launched. That is, one must numerically evolve the curve until the curve reaches the $Z = -z_0$ plane, and then obtain the $P(s_0)$ value found. Such an implicit function ($P(s_0)$ as a function of $|z_0|$) is shown in Figure 3.4b. The cusp-minimums on this plot are the closed MOTS (such as some

of the ones shown in Figure 3.1) where $P(s_0) \rightarrow 0$ (the curve returns to the axis at $Z(s_0) = -z_0$), all other points on this plot indicate MOTOS. The task of finding MOTSs in the abundant sea of MOTOSs now become an optimization problem. Due to the numerically implicit nature of $P(s_0)$ (that is, the MOTSodesic equations are numerically integrated and then a closest-approach radial value is found), a technique called 'random optimization' is employed. Instead of 'brute-forcing' many MOT(O)S initialized with z_0 values systematically chosen to find an implied MOTS, random optimization chooses the z_0 values based on an algorithm that utilizes an aspect of randomness. This technique is more computationally efficient for optimizations of implicit functions, as it drastically reduces the number of computations required to find its extrema. 'Random optimization' is an umbrella term that better known techniques fall under. Our algorithm is inspired by the Metropolis-Hastings algorithms [46], which are often introduced to solve the well-studied Traveling Salesman problem. Figure 3.4c demonstrates a 'minima finder' making its way towards finding the initial z_0 condition to generate the outer-most self-intersecting MOTS shown in Figure 3.2. The number of $P(s_0)$ evaluations between Figures 3.4b and 3.4c is indicative of the heightened efficiency the random optimization provides. This MOTS-finding algorithm will be relied on to generate the results of this thesis in the coming chapter.

A more compact presentation of the MOTSodesic equations can be found in [21, 22], where the authors formulate the curve equations in close analogy to geodesic equations. Further work on generalizing the MOTSodesic equations is seen in [32, 33], for the case of a stationary rotating black hole and higher-dimensional Schwarzschild black hole. However, the interpretations we introduced in the Introduction and this chapter are sufficient for the scope of this thesis.
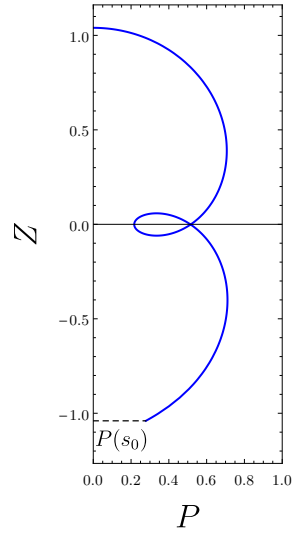
(a) Graphic depiction of the $P(s_0)$ value, which will be minimized (to zero) to find MOTS.
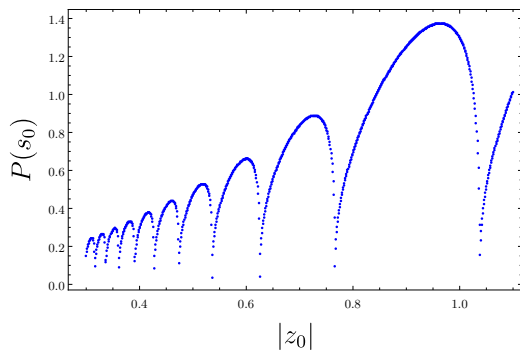
(b) Plot of numerically obtained radial-distance values $P(s_0)$ for a range of z_0.
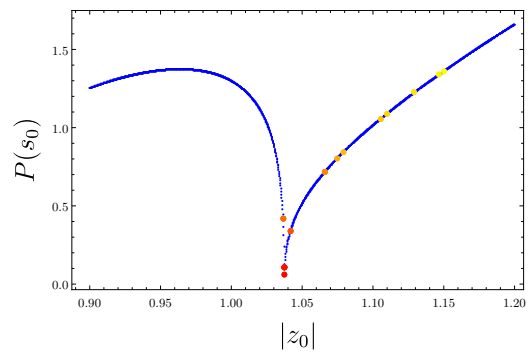
(c) Visualization of a random optimizer's steps towards the minimum.

Figure 3.4: Plots showing the numerical process developed to approximate MOTS.

Chapter 4

Self-intersecting MOTS in other spacetimes

More generally, statically spherical spacetimes have a metric of the form

$$g_{\alpha\beta}\mathrm{d}x^\alpha\mathrm{d}x^\beta = -f(r)\mathrm{d}t^2 + \frac{\mathrm{d}r^2}{f(r)} + r^2\mathrm{d}\Omega^2 \ , \tag{4.1}$$

where $f(r)$ is called the metric function and is constrained only by the Einstein equations. Similarly, the Painlevé–Gullstrand coordinates can be generalized to accommodate for any metric function, with PG-time $\mathrm{d}\tilde{t} = \mathrm{d}t + \frac{\sqrt{1-f}}{f}\mathrm{d}r$ to get

$$g_{\alpha\beta}\mathrm{d}x^\alpha\mathrm{d}x^\beta = -f(r)\mathrm{d}\tilde{t}^2 + 2\sqrt{1-f(r)}\mathrm{d}r\mathrm{d}\tilde{t} + \mathrm{d}r^2 + r^2\mathrm{d}\Omega^2 \ . \tag{4.2}$$

The only non-trivial static spherical asymptotically flat vacuum solution to exist in (3+1) dimensions (by Birkhoff's theorem [7, 34]) is the Schwarzschild solution with the metric function

$$f(r) = 1 - \frac{2M}{r} \ .$$

It can be seen by the line element that the Painlevé–Gullstrand coordinates are valid everywhere since the metric function never exceeds 1 (to render a negative in the square-root term). We will quickly see that the limitation of $f(r) < 1$ voids many non-vacuum solutions of the Einstein equations.

The most well-known non-vacuum solution is that of the matter field defined by a constant $\mathcal{L}_M = \Lambda$, with the metric function taking the form

$$f(r) = 1 - \frac{2M}{r} - \Lambda r^2 \ .$$

The constant Λ is better known as the cosmological constant denoting either an acceleratedly expanding or contracting universe. The expanding solution ($\Lambda > 0$) is de Sitter (dS) space and the contracting one ($\Lambda < 0$) is anti de Sitter (AdS). This example alone demonstrates that for non-vacuum solutions, there are scenarios (such as the AdS case) where the metric function exceeds the value 1. In these cases, the Painlevé–Gullstrand coordinates only cover the spacetime in regions where $f(r) < 1$. However, similarly, many scenarios keep the metric function within the limitation of the Painlevé–Gullstrand coordinates (as with the dS case).

In the following cases (as well as the aforementioned de Sitter spacetime), there are multiple roots to the metric function. Roots of $f(r)$ correspond to spherical MOTSs – in the Schwarzschild case of $f(r) = 1 - 2M/r$, the root at $r = 2M$ is exactly the Schwarzschild radius, the outer-most spherical horizon, the only strictly stable MOTS. The de Sitter spacetime has two roots – the event horizon of the black hole and the cosmological horizon. The cosmological horizon is associated to a boundary of sorts associated with the accelerated expansion of the spacetime. With many cases, it is not always correct to interpret both horizons with trapping properties of light,

as it is better to interpret the physical properties of the horizons using the stability operator (or its eigenvalue spectrum). The horizon associated to the boundary of the black hole is, in our cases, strictly stable and therefore has the 'barrier' property. The other spherical horizons resultant as a root of the metric function do not carry the same characteristic as they are not strictly stable.

This section displays the results of finding self-intersecting MOTSs in non-vacuum black hole solutions such as the 4-dimensional limit of the Gauss–Bonnet (GB) spacetime and the Reissner–Nordstöm black hole. Both of these spacetimes exhibit spherical symmetry and thus may be represented by equation (4.2) with appropriate metric functions. The derivation of MOTSodesic curve equations for axisymmetric MOT(O)Ss is near identical and trivial following the procedures outlined in previous chapters, including but not limited to the limiting approximations near the z axis. The differences in finding and analyzing self-intersecting MOTS arise in that the Painlevé–Gullstrand coordinates may not probe enough of spacetime to find MOTS and there are now non-zero matter terms in the stability operator $G_{ab} \neq 0$. The latter is of less concern, but the former will be addressed when needed.

4.1   Four-Dimensional Gauss–Bonnet Black Hole

One modified theory of gravity that is investigated is the four-dimensional limit of Gauss–Bonnet gravity. Limiting equations of motion to be strictly up to second-order derivatives, the Lovelock theorem states that the Einstein theory (equation (1.2) with $\mathcal{L}_M \propto \Lambda$) is unique to four-dimensions [35]. In higher dimensions, this is no longer true and there are other theories involving higher powers of the curvature that still

admit second-order equations of motion. The simplest such example is Gauss–Bonnet gravity, which exists in five and higher dimensions and involves quadratic powers of the curvature. Recent papers have found a way to take the limit as the dimensionality goes to 4 ($D \to 4$) for these Gauss–Bonnet theories of gravity [36], yielding a theory of gravity that is Einstein with curvature additions:

$$S = \int d^4x \sqrt{-g} \left[R + \alpha \left(\phi \mathcal{G} + 4G^{ab} \partial_a \phi \partial_b \phi - 4 \left(\partial \phi \right)^2 \Box \phi + 2 \left(\partial \phi \right)^4 \right) \right] \ , \qquad (4.3)$$

where $\mathcal{G} = R_{abcd} R^{abcd} - 4R_{ab} R^{ab} + R^2$ is the Gauss–Bonnet invariant, α is the Gauss–Bonnet coupling term (determining the strength of the added curvature terms), and a scalar field ϕ. This theory has second-order equations of motion and evades Lovelock's theory due to the presence of the additional scalar. It is a particular example of a Horndeski theory of gravity [37] that admits solutions agreeing with the naive limit of higher-dimensional Gauss–Bonnet solutions to lower dimensions. This geometry is spherical with a metric function

$$f_{\mathrm{GB}}(r) = 1 + \frac{r^2}{2\alpha} \left(1 - \sqrt{1 + \frac{8\alpha M}{r^3}} \right) \ . \qquad (4.4)$$

The limit as $\alpha \to 0$ recovers the Schwarzschild solution. Figure 4.1 shows its deviation from the Schwarzschild solution. The figure also shows the resolution of the $r = 0$ singularity, as the limit converges $\lim_{r \to 0} f_{\mathrm{GB}} = 0$. The metric function is strictly less than one, thus the Painlevé–Gullstrand coordinates are satisfactory to probe into this black hole. This spacetime's black hole exhibits an outer and inner horizon as there are two roots to f_{GB}

$$r_{\pm} = M \left(1 \pm \sqrt{1 - \frac{\alpha}{M^2}} \right) \ .$$

The spheres of radii $r = r_{\pm}$ are both MOTS. The outermost horizon at $r = r_+$ is the strictly stable MOTS, being the 'barrier' of the black hole and is the apparent
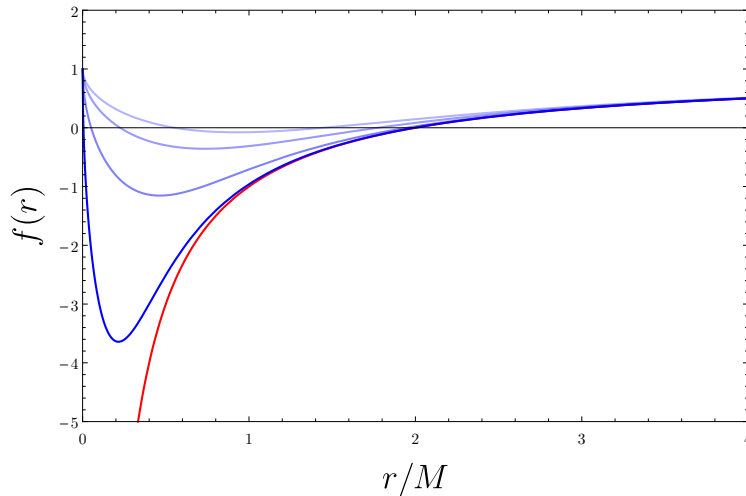
horizon.

Figure 4.1: The Gauss–Bonnet metric function (blue curves) plotted for $\alpha/M^2 = 1/100$, $1/10$, $4/10$, and $8/10$ in order of bottom to top. The red curve is the Schwarzschild metric function.

4.1.1 Self-intersecting MOTS in GB BHs

Our techniques for numerically integrating the MOTSodesic equations, turning it into an optimization problem to find closed MOTS, and then using the pseudo-spectral methods in approximating are replicated to find self-intersecting MOTS within the interior of a GB black hole. The rich interior structure of the GB black hole gives rise to even more interesting self-intersecting MOTS behaviour than those found in the Schwarzschild black hole. In the Schwarzschild limit $\alpha \to 0$, there are seemingly an infinite number of self-intersecting MOTS with a large number of self-intersections. In the extremal limit $\alpha \to M^2$ (where the spherical MOTS coincide $r_- = r_+$), the only MOTS is the degenerate spherical one at $r = M$. In between the two extreme

values of the GB coupling parameter, one finds a limited number of self-intersecting MOTS dependent on the value of α. Furthermore, the structure of the GB black hole seems to sustain pairs of self-intersecting MOTS with the same number of self-intersections providing a simple model where creation/annihilation can be probed. The shape of the twin pairs are very similar, as showcased in Figure 4.2. There are particular values of $0 < \alpha < M^2$ where the self-intersecting twin pairs are coinciding, which can be numerically obtained by many different means. These values are not necessarily relevant to our investigation of self-intersecting MOTSs, but may be of interest and trivially calculated if exact curves describing the self-intersecting MOTS are found.

It is meaningful to consider the eigenvalue spectrum of the stability operator of these surfaces as well. As a function of the α parameter space, we show examples for two pairs of MOTSs – the spherical inner and outer horizons and the twin pairs of the once-self-intersecting MOTSs – in Figures 4.3. By analysis of the three least eigenvalues of the stability operator, we see that only the outer-most MOTS is strictly stable (all positive eigenvalues) and that the inner-horizon has only one negative eigenvalue. Recall that one self-intersection corresponds to at least two negative eigenvalues of the stability operator. At the event of their junction at $\alpha = M^2$, the eigenvalues approach each other with the principal eigenvalue vanishing. The vanishing eigenvalue is expected and aligns with what we understand about the stability operator and these MOTSs. The eigenvalue spectrum for the one-self-intersecting pair of MOTSs is as expected as well – there are at least two negative eigenvalues (λ_0 and λ_1) with the interior once-intersecting MOTS carrying a third negative eigenvalue. At the point at which the pair coincides $\alpha \approx 0.1359915193M^2$, we again see a vanishing

eigenvalue, but this time the third eigenvalue λ_2. This spectral analysis was also done but not presented for the twice- and thrice-self-intersecting pairs of MOTSs where the pattern continues (with vanishing λ_4 and λ_6, respectively, at the point of their 'annihilations'). This phenomenon is expected to extend to the infinitely many self-intersecting pairs MOTSs anticipated as $\alpha \to 0$.
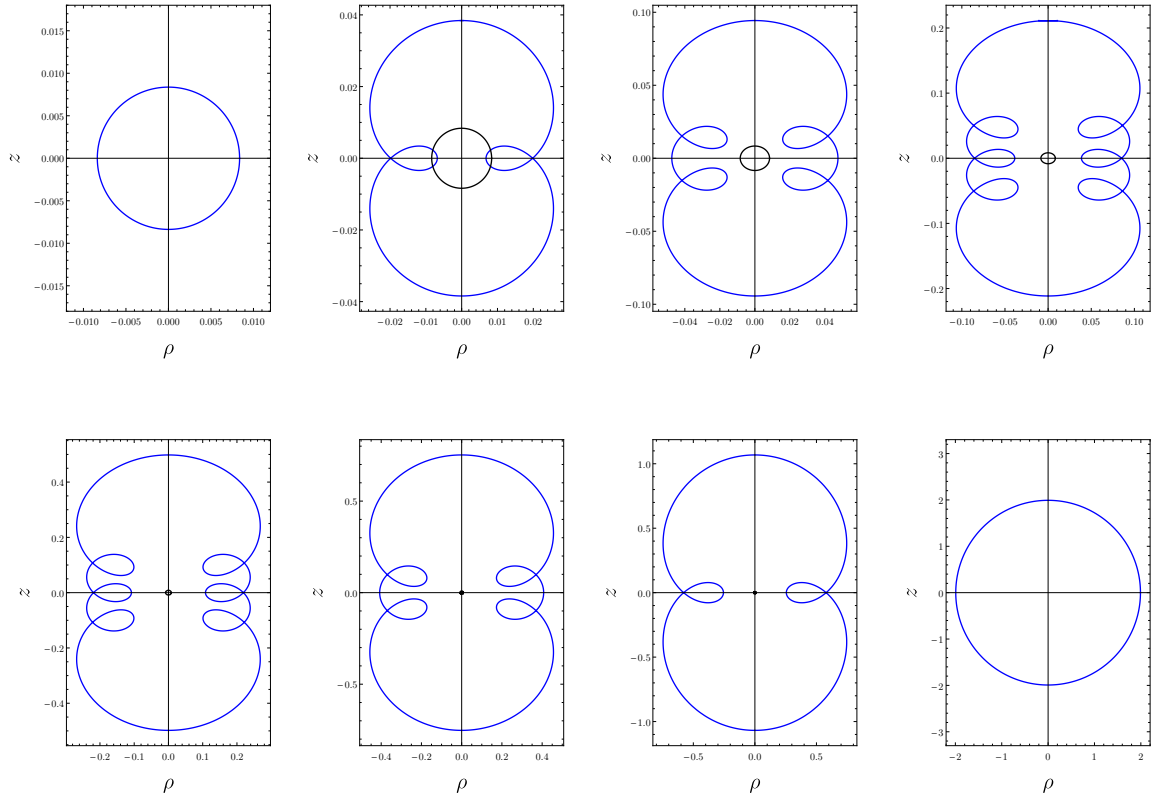

Figure 4.2: All axisymmetric MOTSs present in the GB black hole in the case $\alpha/M^2 = 1/60$. Note that the scale changes in the plots for the purposes of visibility. The inner horizon has been included as a black circle to provide scale.
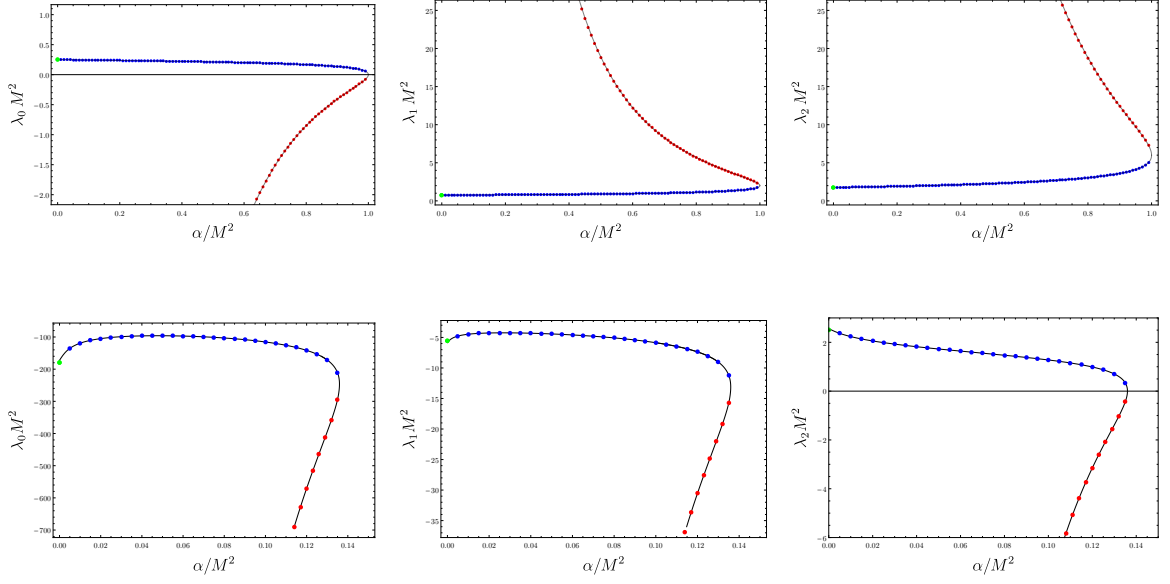
Figure 4.3: First three eigenvalues of the stability operator as a function of the coupling parameter for the outer (blue) and inner (red) horizons (top) and once-intersecting MOTS (bottom) for the GB spacetime. The black curve is an interpolation of the numerically obtained data, while the dots are a few of the numerically determined values. The green dots correspond to the respective eigenvalue in the Schwarzschild case, as obtained separately.

4.2   Reissner–Nordström Black Hole

The next spacetime of interest to be investigated is the Reissner–Nordström (RN) spacetime which is a solution of the Einstein-Maxwell equations. The RN black hole is a solution of Einstein gravity coupled to Maxwell electrodynamics, namely using the Faraday tensor $F_{\alpha\beta}$:

$$S = \int d^4x \sqrt{-g} \left(R - F_{\alpha\beta}F^{\alpha\beta} \right) \ . \tag{4.5}$$

Physically, this is electromagnetism in a curved spacetime. The solution to the Einstein's equations once again takes a spherical form with a metric function

$$f_{\mathrm{RN}}(r) = 1 - \frac{2M}{r} + \frac{Q^2}{r^2} \, , \tag{4.6}$$

where Q is a charge parameter. Once again, there are two horizons (inner and outer, from two roots of $f_{\mathrm{RN}}(r)$, refer to Figure 4.4) at

$$r_{\pm} = M \pm \sqrt{M^2 - Q^2} \, .$$

The extreme case of $Q^2 = M^2$ is once again where the inner and outer horizons coincide. The $Q^2 > M^2$ case is that of a naked singularity, which we will avoid and consider only $0 < M < |Q|$.
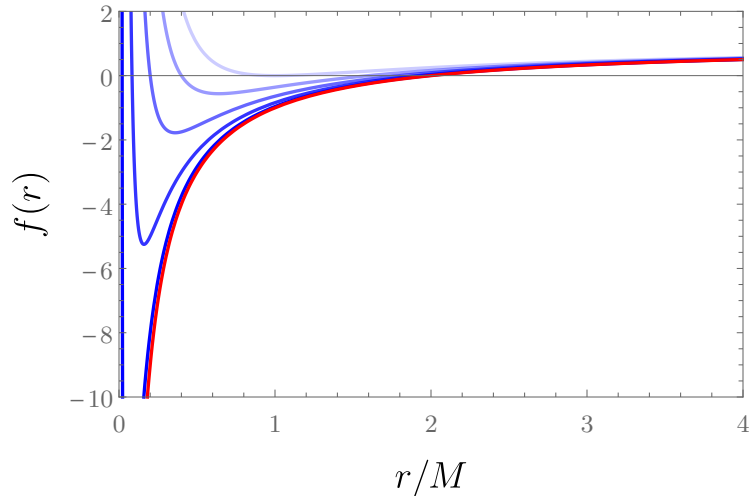

Figure 4.4: The Reissner–Nordström metric function (blue curves) plotted for $Q^2/M^2 = 0.2$, 0.4, 0.6, 0.8, and 1 in order of bottom to top. The red curve is the Schwarzschild metric function.

In a sense, the charged black hole has repulsive gravity near the $r = 0$ singularity.

From the metric function as well, we see it is not strictly less than 1, rendering the Painlevé–Gullstrand coordinates invalid for regions where $f_{\mathrm{RN}}(r) \geq 1$. Coordinates that generalize the PG coordinates such as [38] are not sufficient to fully probe these spacetimes, thus we find a further generalization of said coordinates.

4.2.1 Further generalized Painlevé–Gullstrand coordinates

Begin with the null coordinates (transform Equation (4.1) via $\mathrm{d}t \to \mathrm{d}v - \mathrm{d}r/f$):

$$g_{\alpha\beta}\mathrm{d}x^\alpha\mathrm{d}x^\beta = -f\mathrm{d}v^2 + 2\mathrm{d}v\mathrm{d}r + r^2\mathrm{d}\Omega^2 \tag{4.7}$$

and then perform the coordinate transformation

$$v = \tau + g(r) \implies \mathrm{d}v = \mathrm{d}\tau + g'\mathrm{d}r$$

with $g(r)$ being an arbitrary function. This leaves us with

$$g_{\alpha\beta}\mathrm{d}x^\alpha\mathrm{d}x^\beta = -f\mathrm{d}\tau^2 + 2(1 - g' \cdot f)\mathrm{d}\tau\mathrm{d}r + g' \cdot (2 - g' \cdot f)\mathrm{d}r^2 + r^2\mathrm{d}\Omega^2 \ .$$

Using the identification

$$p(r) \equiv g' \cdot (2 - g' \cdot f) \tag{4.8}$$

makes the line element a lot cleaner:

$$g_{\alpha\beta}\mathrm{d}x^\alpha\mathrm{d}x^\beta = -f\mathrm{d}\tau^2 + 2\sqrt{1 - p(r)f(r)}\mathrm{d}\tau\mathrm{d}r + p(r)\mathrm{d}r^2 + r^2\mathrm{d}\Omega^2 \ . \tag{4.9}$$

Thanks to the arbitrary choice of $g(r)$, $p(r)$ is essentially arbitrary as well. It is restricted only by the constraint of $p(r) > 0$ (so that the constant time slices are space-like) and to ensure that $1 - pf > 0$.

Although the choice of $p(r)$ is arbitrary, it can be understood as describing the kinematics of observers whose 4-velocity is tangent to $\frac{\partial}{\partial\bar{t}}$. For Painlevé–Gullstrand

coordinates, such an observer was free-falling. In the generalization, the observer is radially accelerating with acceleration

$$|a| = \frac{|p'|}{2p^{3/2}} \; .$$

In the case of the charged black hole, there is a natural choice for $p(r)$ – that of a test particle oppositely charged to the black hole and so is attractively accelerated towards the singularity through the Lorentz force. This choice is

$$p(r) = \frac{r^2}{(r - \mu Q)^2} \; , \tag{4.10}$$

where Q is the black hole charge and μ is the charge to mass ratio of the test particle. This choice of p also dictates a zero initial velocity v_∞ at $r \to \infty$:

$$v_\infty = \sqrt{1 - \lim_{r \to \infty} p(r)} = 0 \; .$$

Most importantly, this choice of $p(r)$ assures that the coordinates (4.9) are valid for $r \in (0, \infty)$. Taking $Q > 0$ and assigning $\mu = -1$, the line element is explicitly:

$$g_{\alpha\beta} \mathrm{d}x^\alpha \mathrm{d}x^\beta = -\left(1 - \frac{2M}{r} + \frac{Q^2}{r^2}\right) \mathrm{d}\tau^2 + \sqrt{\frac{(M+Q)r}{2(r+Q)^2}} \mathrm{d}\tau \mathrm{d}r + \frac{r^2 \mathrm{d}r^2}{(r+Q)^2} + r^2 \mathrm{d}\Omega^2 \; . \tag{4.11}$$

One has to be careful when looking at plots of MOTS generated on this set of co-ordinates. The slicings of constant τ are not Euclidean – meaning that the usual identifications between polar and cartesian coordinates are not the same, since there is now a functional scaling in the radial coordinate. Our analysis of self-intersecting MOTSs within the Reissner–Nordström black hole is qualitative when it comes to displaying their plots, thus this feature is ignored. A remedy, however, is possible by performing yet another coordinate transformation such that we arrive at a set of

coordinates that fully cover the spacetime and are conformally Euclidean such that our plots are accurate in the Cartesian graph.

The coordinates (4.9) are referred to as the 'further generalized Painlevé–Gullstrand' coordinates as the authors of [38] have already taken the 'generalization' title. This generalization is motivated by [38].

4.2.2 Self-intersecting MOTS in RN BHs

Once again, the procedure in forming the MOTSodesic equations mirror the techniques introduced in Chapter 1 with normal one-forms and vectors

$$u_\alpha \mathrm{d}x^\alpha = \frac{-\mathrm{d}\tau}{\sqrt{p(r)}} \qquad \text{and} \qquad n^\alpha \frac{\partial}{\partial x^\alpha} = r\sqrt{p(r)} \left[\frac{\dot{\theta}}{p(r)} \frac{\partial}{\partial r} - \frac{\dot{r}}{r^2} \frac{\partial}{\partial \theta} \right] . \qquad (4.12)$$

Similar to the MOTSs found within the GB black hole, the richer structure within the black hole sets a limit on the number of self-intersecting axisymmetric MOTSs.

The complexity of the possible axisymmetric MOTSs in the GB black holes pales beside that of the RN black holes. The results of self-intersecting MOTSs found and their analysis are showcased in Figures 4.5 through 4.10. Firstly, there are features of the parameter space that appear to transition MOTSs from self-intersecting to non-intersecting regimes. In the plots of Figure 4.5, the once- and twice-intersecting MOTSs grow sharper as Q increases. An intermediary MOTS (purple) seems to appear in a creation-bifurcation event together with a sharp but non-intersecting MOTS (in red), where the intermediary MOTS annihilates with the self-intersecting MOTS and the other MOTS (red) progresses to coincide with the inner horizon. This is true in both the once- and twice-intersecting cases. The convolution of these 'evolutions' prompts a way of tracking these surfaces through the parameter space.
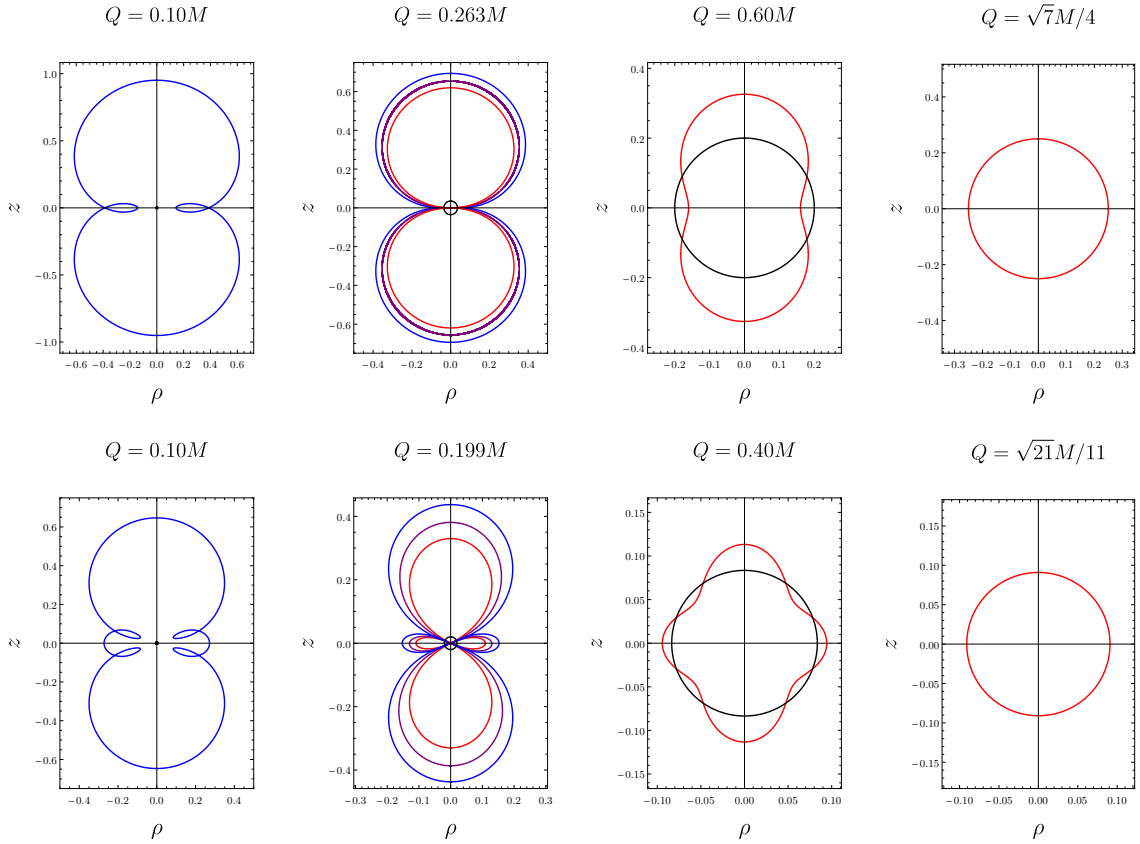
Figure 4.5: Snapshots of the once- and twice-intersecting MOTSs in varying parameter values of Q. In all cases, the black circle corresponds to the inner horizon. The MOTSs are plotted in coordinates $(\rho, z) = (r \cos \theta, r \sin \theta)$.

The area of the MOTSs will be calculated and plotted as done in Figure 4.6 for the once-intersecting MOTS. The corresponding MOTSs are shown in the plots of Figure 4.7. One sees that there are, in fact, two creation-annihilation events that unfold for this class of MOTS (between the blue-purple-red curves and green-red curves), which show up on these area-plots as 'S's. Ultimately, the once-intersecting MOTS ceases to exist past the charge parameter value of $Q \approx 0.7464488M$. The green MOTS that is paired and annihilates with the 'evolution' of the once-intersecting MOTS is tracked
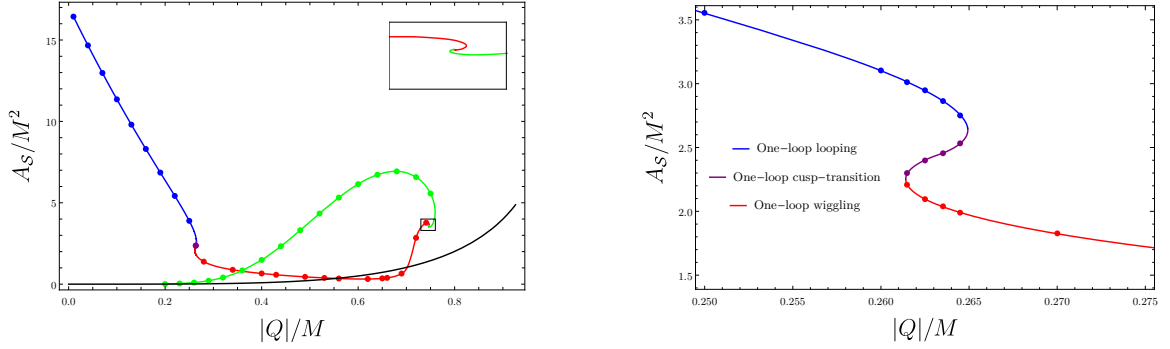
Figure 4.6: Left: The area of the once-intersecting MOTS found in spacetimes of varying parameter Q. The black curve gives the area of the inner horizon. The inset shows a zoomed-in version of the region highlighted with the small black hole. The different colors (blue, red, green, purple) correspond to the MOTSs displayed in Figure 4.7. Right: A zoomed-in version of the top plot, focussing on the region where the once-intersecting surface loses its intersecting feature.

to be linked to the twice-intersecting MOTS (as shown in the bottom-right plot of Figure 4.6. The other (infinitely many) intersecting MOTSs undergo similar fates, as demonstrated by the thrice-intersecting MOTS's 'evolution' in Figure 4.10, with a key difference being that the blue-purple-red interaction found in the once-intersecting is enhanced to more intermediary MOTSs that are involved in the transition (blue-cyan-purple-violet-red). This is expected to generally increase every two self-intersections present for this phenomenon found in the Reissner–Nordström spacetime.

The eigenvalue spectra of the stability operator was also calculated and examined. The spectra for the once-intersecting MOTSs is shown through its 'evolution' through Q in Figures 4.9 and 4.8. The principal eigenvalue tends to large values, as shown in 4.9. The plots in Figure 4.8 further support the observations that there is a
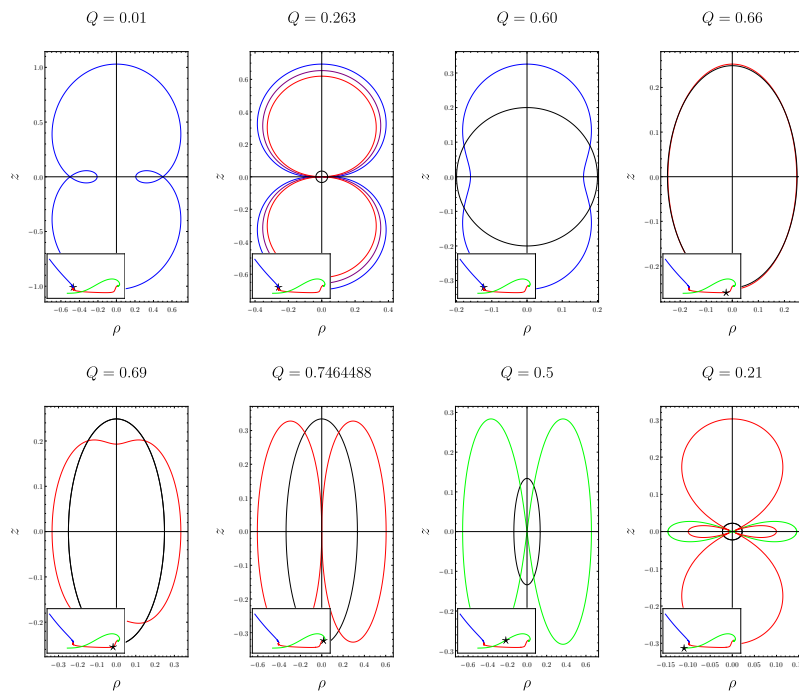
50

Figure 4.7: Snapshots of the once-intersecting MOTS's 'evolution' through the charge parameter space. In all cases, the black circle corresponds to the inner horizon. The MOTSs are plotted in coordinates $(\rho, z) = (r \cos \theta, r \sin \theta)$.

vanishing (non-principal) eigenvalue that vanishes in the event of coinciding surfaces. This is demonstrated in the final annihilation of the once-intersecting MOTS (on the top-left plot, where the green λ_1 eigenvalue goes to zero and then ceases to exist) and in the creation-then-annihilation (blue-purple-red) interaction where λ_2 vanishes (on the bottom plots). The author also cautions against believing all coincidences of overlapping MOTSs to be creation or annihilation events, as all the intersecting MOTSs "phases through" the inner horizon to be annihilated somewhere else.
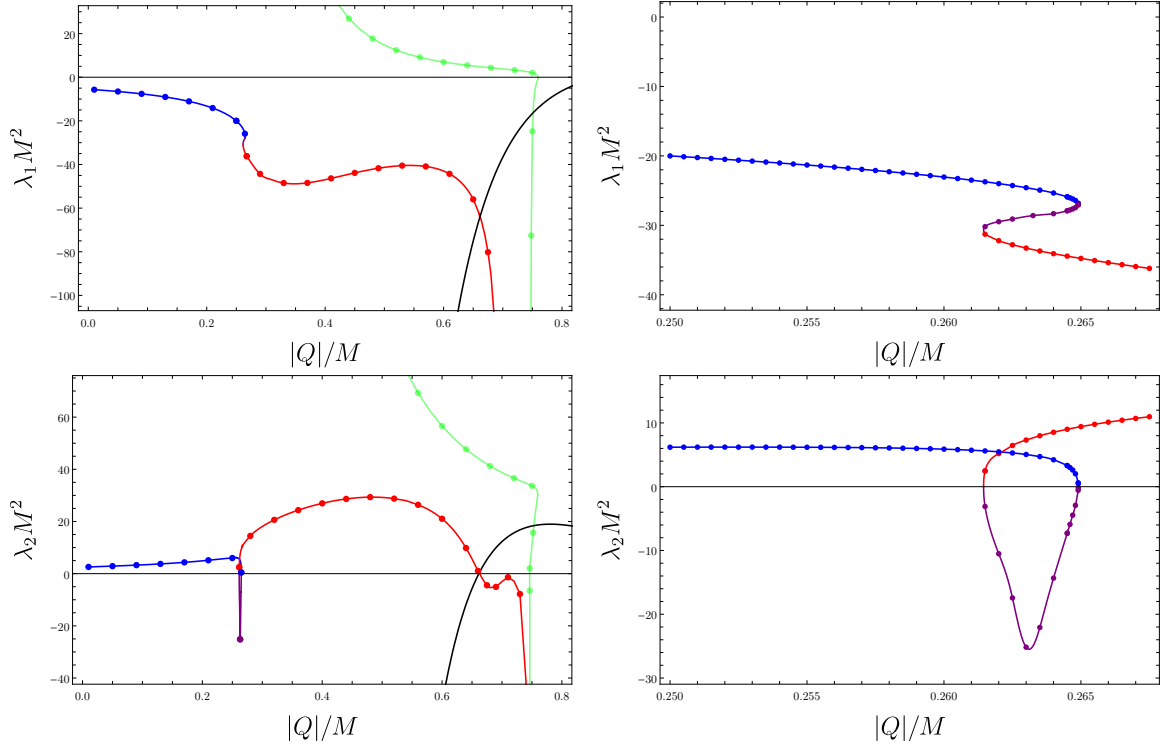
Figure 4.8: Plots of the $\ell = 1$ (top) and $\ell = 2$ (bottom) eigenvalues of the once-intersecting MOTS for varying charge parameter. The right plots provide a zoomed-in view of the corresponding left plot over a region of interest. The black curve corresponds to the corresponding eigenvalue of the inner horizon of the black hole. In the left panels, the red and green curves eventually meet, though this occurs at such large values of the eigenvalues that displaying it would obscure the more interesting structures shown here.
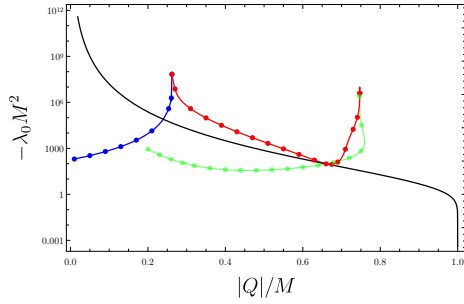
Figure 4.9: A plot of (the negative of) the principal eigenvalue of the stability operator for the once-intersecting surface in the Reissner–Nordström spacetime. The principal eigenvalue exhibits strong peaks at the location of cusps. The black curve corresponds to the principal eigenvalue of the inner horizon of the black hole.
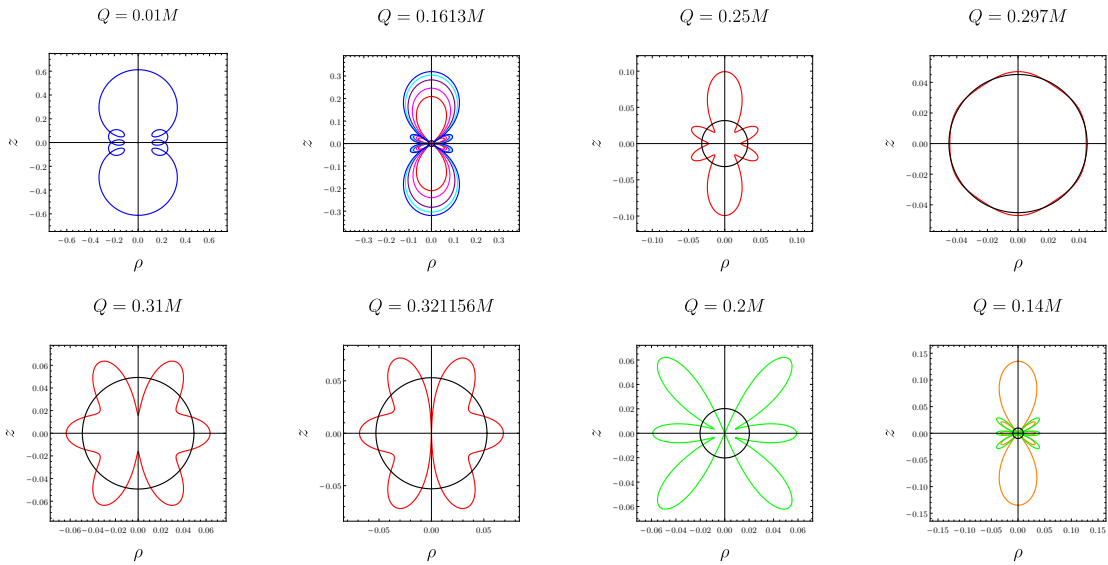
Figure 4.10: Snapshots of the thrice-intersecting MOTS's 'evolution' through the charge parameter space. In all cases, the black circle corresponds to the inner horizon. The MOTSs are plotted in coordinates $(\rho, z) = (r\cos\theta, r\sin\theta)$.

53

Chapter 5

Discussion & Conclusion

The now extended understanding of black hole mergers and the existence of self-intersecting MOTSs in static black holes have been presented in this thesis. Clearly, we then need methods to effectively track the many surfaces that are now understood to exist. We have presented working numerical techniques to find such exotic MOTSs and track them through their evolution through parameter space. This was trivially extended to find and evolve the MOTSs through time in other works – such as those in the black hole merger evolution. It was common to display all the MOTSs by their area (such as Figure 2.5), but in light of recent findings (including from the works in this thesis) regarding vanishing non-principal eigenvalues indicating the annihilation of the MOTS, plots showing the evolution of the eigenvalues are more suited for self-intersecting MOTSs, particularly when the number of MOTSs reaches a large number (such as in Figure 2.7). This thesis has provided more examples in which non-principal eigenvalues vanish in their annihilation events. However, one must remember that the 'evolution' of the spacetimes we investigated are not dynamical. If these were

dynamical black holes, by [25] and [22], if $\mathcal{S}$ does not evolve (in time) smoothly, then either

1. $\mathcal{S}$ is smooth but the stability operator has a vanishing eigenvalue; or

2. $\mathcal{S}$ is not smooth (has a cusp).

The spacetimes we dealt with are not applicable with these statements, but resembles them. Although a vanishing non-principal eigenvalue is likely indicative of a non-smooth evolution through parameter space (such as their abrupt annihilation as we vary parameter values Q and α), there are examples of the MOTS 'phasing through' another surface, giving us the vanishing eigenvalue at the point of overlap (such as in the Reissner–Nordström spacetime when the MOTSs 'phases through' the inner horizon).

The cause of the self-intersections in these MOTSs are not clear. In the MOTSodesic equations, there are clear repulsive terms in the Schwarzschild case that drive the curves away from the z-axis. The different types of MOTSs and limitation on how many were found in the presence of an inner horizon gives a little insight and allows some hypotheses to be drawn. One idea is that the depth of the metric function would dictate how many axisymmetric MOTSs would be found, similar to quantum energy levels from potential energy curves in an atom. Since the Schwarzschild metric tends to $-\infty$ as $r \to 0$, this would explain the infinitely many MOTSs found. This was not a topic that we investigated thoroughly as such arguments are rooted in numerical examples rather than mathematical proofs. In leaving the realm of physical validity, it would be meaningful to investigate such a limitation for an arbitrary choice of the metric function ($f(r)$), ignoring the constraints of Einstein's field equations (1.3).

More hypotheses have been formed outside the scope of this paper – one being that the self-intersecting MOTSs are resultant of the departure from time-symmetry. This can be tested using Kruskal-Szekeres (KS) coordinates on the Schwarzschild spacetime, where constant KS-time (T) slices change with time (T is not a direction of symmetry in the spacetime). This is ongoing work that uses the same MOTS finding techniques outlined in this thesis to track MOTSs through KS time.

The importance of the further generalized Painlevé–Gullstrand coordinates should not be overlooked. This set of coordinates allows for the thorough probing beyond the inner horizon of many black holes that have had such limitations. One may imagine, for example, that if they were to calculate quantum perturbations in these spacetimes that they would rather have access to the global manifold rather than a subset. Concerns such as these are typically individually dealt with (see [39, 40]), but we have now provided another tool to do such probes.

In particular, we are interested in using this extension to coordinates on AdS spacetimes. AdS spacetimes are of interest largely owing to the holographic theories regarding it [41]. The AdS/CFT correspondence provides a dictionary between anti de Sitter space and a *conformal field theory* (CFT) of one dimension less. For example, thermodynamic properties such as entropy and temperature of the system in the CFT is associated to the area and surface gravity of geometrical objects in the AdS spacetime [42]. In many cases, the many body problem in the CFT is vastly more simple to compute using the associated geometry. The further generalized Painlevé–Gullstrand coordinates can also be extended to encompass similarly problematic rotating black holes, as done in [43]. The Kerr spacetime describes these black holes. Introducing a component of angular momentum makes the models more astrophysically relevant,

as all black holes are expected to spin.

At the end of the day, the self-intersecting MOTSs showcased here are geometric objects found within black holes that have uncertain physical implications – as in, it is not clear what an observer would experience if one passes through one of these self-intersecting surfaces. The apparent horizon is well known and popularly understood with its light-trapping property, but the self-intersecting MOTSs within need further understanding. One feature that is lacking is that of an analytical form for the MOTS $\mathcal{S}(s, \phi)$ as we have only found self-intersecting MOTSs through numerical solutions to the differential equations describing the MOTSs. This is not as large of an issue as with numerical techniques and enough computational power in an average personal computer, the solving and analyzing of MOTSs is doable with meaningful results. One benefit of our work in static analytical spacetimes provides a rough 'initial data' MOTS-shape for the same investigations to be done on numerically computed spacetimes. These calculations require large computational clusters as are done in [18–20, 22]. The analysis of self-intersecting MOTSs (particularly with the stability operator) extends to properties found in the dynamic case. To that end, self-intersecting MOTSs in analytically dynamic spacetimes (such as the Vaidya or Lemaître–Tolman–Bondi spacetimes) may be interesting to investigate.

The problem of the fate of the original two apparent horizons during a binary black hole merger event has been numerically resolved, and their annihilation seems to include self-intersecting surfaces. This new phenomenon of self-intersecting MOTSs is still very unclear, particularly from the physical context, despite now many numerical results showing their robustness in multiple models satisfying the Einstein equations. The work of this thesis progresses our understanding of these self-intersecting MOTSs,

as we have showcased the same self-intersecting feature in our numerical MOTSs. By 'evolving' the MOTSs through the parameter space, the results of the eigenvalue spectra adds evidence to vanishing non-principal eigenvalues in annihilation events as first found in [22].

Bibliography

[1] R. Penrose, "Gravitational collapse and space-time singularities," Phys. Rev. Lett. **14**, 57–59 (1965).

[2] A. M. Ghez, S. Salim, N. N. Weinberg, J. R. Lu, T. Do, J. K. Dunn, K. Matthews, M. R. Morris, S. Yelda, E. E. Becklin, T. Kremenek, M. Milosavljevic, and J. Naiman, "Measuring distance and properties of the milky way's central super-massive black hole with stellar orbits," The Astrophysical Journal **689**, 1044–1062 (2008).

[3] E. H. T. Collaboration, "First sagittarius a* event horizon telescope results. i. the shadow of the supermassive black hole in the center of the milky way," The Astrophysical Journal Letters **930**, L12 (2022).

[4] E. H. T. Collaboration, "First m87 event horizon telescope results. i. the shadow of the supermassive black hole," The Astrophysical Journal Letters **875** (2019).

[5] C. W. Misner, K. S. Thorne, and J. A. Wheeler, *Gravitation* (1973).

[6] J. B. Hartle, *Gravity : an introduction to Einstein's general relativity* (2003).

[7] E. Poisson, *A relativist's toolkit : the mathematics of black-hole mechanics* (2004).

[8] S. W. Hawking and G. F. R. Ellis, *The large-scale structure of space-time.* (1973).

[9] M. Visser, "Physical observability of horizons," Phys. Rev. D **90**, 127502 (2014), arXiv:1407.7295 [gr-qc] .

[10] T. L. S. Collaboration and T. V. Collaboration, "Observation of Gravitational Waves from a Binary Black Hole Merger," Phys. Rev. Lett. **116**, 061102 (2016), arXiv:1602.03837 [gr-qc] .

[11] S. G. Hahn and R. W. Lindquist, "The two-body problem in geometrodynamics," Annals of Physics **29**, 304–331 (1964).

[12] M. Alcubierre, *Introduction to 3+1 Numerical Relativity* (2008).

[13] F. Pretorius, "Evolution of Binary Black-Hole Spacetimes," Physical Review Letters **95**, 121101 (2005), arXiv:gr-qc/0507014 [gr-qc] .

[14] R. A. Matzner, H. E. Seidel, S. L. Shapiro, L. Smarr, W. M. Suen, S. A. Teukolsky, and J. Winicour, "Geometry of a Black Hole Collision," Science **270**, 941–947 (1995).

[15] J. Thornburg, "A fast apparent horizon finder for three-dimensional cartesian grids in numerical relativity," Classical and Quantum Gravity **21**, 743–766 (2003).

[16] "The einstein toolkit," (2022), to find out more, visit http://einsteintoolkit.org.

[17] A. Gupta, B. Krishnan, A. B. Nielsen, and E. Schnetter, "Dynamics of marginally trapped surfaces in a binary black hole merger: Growth and approach to equilibrium," Phys. Rev. D **97**, 084028 (2018), arXiv:1801.07048 [gr-qc] .

[18] D. Pook-Kolb, O. Birnholtz, B. Krishnan, and E. Schnetter, "Existence and stability of marginally trapped surfaces in black-hole spacetimes," Phys. Rev. D **99**, 064005 (2019).

[19] D. Pook-Kolb, O. Birnholtz, B. Krishnan, and E. Schnetter, "Interior of a Binary Black Hole Merger," Phys. Rev. Lett. **123**, 171102 (2019), arXiv:1903.05626 [gr-qc] .

[20] D. Pook-Kolb, O. Birnholtz, B. Krishnan, and E. Schnetter, "Self-intersecting marginally outer trapped surfaces," Phys. Rev. D **100**, 084044 (2019), arXiv:1907.00683 [gr-qc] .

[21] I. Booth, R. A. Hennigar, and D. Pook-Kolb, "Ultimate fate of apparent horizons during a binary black hole merger. I. Locating and understanding axisymmetric marginally outer trapped surfaces," Phys. Rev. D **104**, 084083 (2021), arXiv:2104.11343 [gr-qc] .

[22] D. Pook-Kolb, I. Booth, and R. A. Hennigar, "Ultimate fate of apparent horizons during a binary black hole merger. II. The vanishing of apparent horizons," Phys. Rev. D **104**, 084084 (2021), arXiv:2104.11344 [gr-qc] .

[23] J. Stoer and R. Bulirsch, *Introduction to Numerical Analysis*, Texts in applied mathematics (Springer-Verlag, 1993).

[24] L. Andersson, M. Mars, and W. Simon, "Stability of marginally outer trapped surfaces and existence of marginally outer trapped tubes," arXiv e-prints , arXiv:0704.2889 (2007), arXiv:0704.2889 [gr-qc] .

[25] L. Andersson, M. Mars, and W. Simon, "Local Existence of Dynamical and Trapping Horizons," Physical Review Letters **95**, 111102 (2005), arXiv:gr-qc/0506013 [gr-qc] .

[26] I. Booth and S. Fairhurst, "Isolated, slowly evolving, and dynamical trapping horizons: Geometry and mechanics from surface deformations," Physical Review D **75**, 084019 (2007), arXiv:gr-qc/0610032 [gr-qc] .

[27] J. P. Boyd, *Chebyshev and Fourier Spectral Methods*, 2nd ed., Dover Books on Mathematics (Dover Publications, Mineola, NY, 2001).

[28] C. Canuto, M. Hussaini, A. Quarteroni, and T. Zang, *Spectral Methods: Fundamentals in Single Domains*, Scientific Computation (Springer Berlin Heidelberg, 2009).

[29] B. Steltner, T. Menne, M. A. Papa, and H. B. Eggenstein, "Density-clustering of continuous gravitational wave candidates from large surveys," Physical Review D **106**, 104063 (2022), arXiv:2207.14286 [gr-qc] .

[30] B. Steltner, M. A. Papa, H. B. Eggenstein, R. Prix, M. Bensch, and B. Machenschalk, "Deep Einstein@Home all-sky search for continuous gravitational waves in LIGO O3 public data," arXiv e-prints , arXiv:2303.04109 (2023), arXiv:2303.04109 [gr-qc] .

[31] I. Booth, R. A. Hennigar, and S. Mondal, "Marginally outer trapped surfaces in the Schwarzschild spacetime: Multiple self-intersections and extreme mass ratio mergers," Phys. Rev. D **102**, 044031 (2020), arXiv:2005.05350 [gr-qc] .

[32] I. Booth, K. T. B. Chan, R. A. Hennigar, H. Kunduri, and S. Muth, "Exotic marginally outer trapped surfaces in rotating spacetimes of any dimension," arXiv e-prints , arXiv:2210.15685 (2022), arXiv:2210.15685 [gr-qc] .

[33] S. M. MacDonald Muth, *Marginally outer trapped (open) surfaces in 4+1 dimensional spacetimes*, Master's thesis, Memorial University of Newfoundland (2021).

[34] R. M. Wald, *General Relativity* (1984).

[35] D. Lovelock, "The Einstein tensor and its generalizations," J. Math. Phys. **12**, 498–501 (1971).

[36] R. A. Hennigar, D. Kubizňák, R. B. Mann, and C. Pollack, "On taking the d → 4 limit of gauss-bonnet gravity: theory and solutions," Journal of High Energy Physics **2020** (2020), 10.1007/jhep07(2020)027.

[37] H. Lü and Y. Pang, "Horndeski gravity as D → 4 limit of Gauss-Bonnet," Physics Letters B **809**, 135717 (2020), arXiv:2003.11552 [gr-qc] .

[38] K. Martel and E. Poisson, "Regular coordinate systems for schwarzschild and other spherical spacetimes," American Journal of Physics **69**, 476–480 (2001).

[39] G. Volovik, "Painlevé–gullstrand coordinates for schwarzschild–de sitter spacetime," Annals of Physics **449**, 169219 (2023).

[40] Q.-Q. Jiang and S.-Q. Wu, "Hawking radiation of charged particles as tunneling from Reissner Nordström de Sitter black holes with a global monopole," Physics Letters B **635**, 151–155 (2006), arXiv:hep-th/0511123 [hep-th] .

[41] J. Maldacena, "The large-n limit of superconformal field theories and supergravity," International journal of theoretical physics **38**, 1113–1133 (1999).

[42] M. Rangamani and T. Takayanagi, *Holographic Entanglement Entropy* (Springer International Publishing, 2017).

[43] I. Booth, K. T. B. Chan, R. A. Hennigar, H. Kunduri, and S. Muth, "Exotic marginally outer trapped surfaces in rotating spacetimes of any dimension," (2022), arXiv:2210.15685 [gr-qc] .

[44] D. Pook-Kolb, O. Birnholtz, J. L. Jaramillo, B. Krishnan, and E. Schnetter, "Horizons in a binary black hole merger I: Geometry and area increase," arXiv e-prints , arXiv:2006.03939 (2020), arXiv:2006.03939 [gr-qc] .

[45] D. Pook-Kolb, O. Birnholtz, J. L. Jaramillo, B. Krishnan, and E. Schnetter, "Horizons in a binary black hole merger II: Fluxes, multipole moments and stability," arXiv e-prints , arXiv:2006.03940 (2020), arXiv:2006.03940 [gr-qc] .

[46] W. H. Press, S. A. Teukolsky, W. T. Vetterling, and B. P. Flannery, *Numerical Recipes 3rd Edition: The Art of Scientific Computing*, 3rd ed. (Cambridge University Press, USA, 2007).

Appendix A

Calculations: Null Geodesics of the Schwarzschild spacetime

This is an exercise commonly given to undergraduate students in GR, but an explicit calculation will be shown that gives us null geodesic curves in closed form when considering the Schwarzschild spacetime in both the Schwarzschild coordinates and Painlevé-Gullstrand coordinate charts.

A.1 Null geodesics in the Schwarzschild chart

A null curve $\{\gamma : x^\alpha\}$ is such that $g_{\alpha\beta}\frac{\mathrm{d}x^\alpha}{\mathrm{d}\lambda}\frac{\mathrm{d}x^\beta}{\mathrm{d}\lambda} = 0$, where λ is a parameter along the curve. For a strictly radial geodesic, $x^\theta = x^\phi = 0$, leaving

$$g_{\alpha\beta}\frac{\mathrm{d}x^\alpha}{\mathrm{d}\lambda}\frac{\mathrm{d}x^\beta}{\mathrm{d}\lambda} = -\left(1 - \frac{2M}{r}\right)\left(\frac{\mathrm{d}t}{\mathrm{d}\lambda}\right)^2 + \left(1 - \frac{2M}{r}\right)^{-1}\left(\frac{\mathrm{d}r}{\mathrm{d}\lambda}\right)^2$$

The null curve can be solved analytically for a closed-form $t(r)$:

$$0 = -\left(1 - \frac{2M}{r}\right)\left(\frac{\mathrm{d}t}{\mathrm{d}\lambda}\right)^2 + \left(1 - \frac{2M}{r}\right)^{-1}\left(\frac{\mathrm{d}r}{\mathrm{d}\lambda}\right)^2$$

$$\mathrm{d}t^2 = \frac{\mathrm{d}r^2}{(1 - 2M/r)^2}$$

$$t_{(\gamma)}(r) = \pm\left(r + 2M\ln(r - 2M)\right) + C$$

The negative solution is the path of an in-falling null observer for $r > 2M$ (the integration constant C can be varied for appropriate initial conditions).

A.2 Null geodesics in the Painlevé–Gullstrand chart

Repeating the calculation but from the perspective of the $\{\tilde{t}, r\}$ chart:

$$\tilde{g}_{\alpha\beta}\frac{\mathrm{d}x^\alpha}{\mathrm{d}\lambda}\frac{\mathrm{d}x^\beta}{\mathrm{d}\lambda} = -\left(1 - \frac{2M}{r}\right)\left(\frac{\mathrm{d}\tilde{t}}{\mathrm{d}\lambda}\right)^2 + 2\sqrt{2M/r}\left(\frac{\mathrm{d}\tilde{t}}{\mathrm{d}\lambda}\right)\left(\frac{\mathrm{d}r}{\mathrm{d}\lambda}\right) + \left(\frac{\mathrm{d}r}{\mathrm{d}\lambda}\right)^2$$

$$0 = -\left(1 - \frac{2M}{r}\right)\mathrm{d}\tilde{t}^2 + 2\sqrt{2M/r}\,\mathrm{d}\tilde{t}\,\mathrm{d}r + \mathrm{d}r^2$$

$$\mathrm{d}\tilde{t} = \frac{\mathrm{d}r}{\left(\pm 1 - \sqrt{2M/r}\right)} = \pm\frac{\mathrm{d}r}{1 - 2M/r} + \frac{\sqrt{2M/r}}{1 - 2M/r}\mathrm{d}r$$

This curve takes a familiar form, where the first term is the same as the equation in Schwarzschild coordinates and the second term is exactly the term involved in the coordinate transformation between Schwarzschild and PG coordinates (Eqn. (1.7)).

$$\tilde{t}_{(\gamma)}(r) = \pm r - 2M\ln\left(\frac{r + 2M + 2\sqrt{2Mr}}{(r - 2M)^{1\pm 1}}\right) + 2\sqrt{2Mr} + C$$

The terms come together to deal with the cause of the divergence at $r = 2M$ for the in-going null geodesic choice ($\pm = -$), but the blow-up remains for out-going null geodesics ($\pm = +$) as one would expect from the 'trapping' nature of the black hole.

Appendix B

Snippets of Code: Automated MOTS-finding

One is able to numerically integrate the MOTSodesic equations simply using their favourite ODE-solving packages. The author's package of choice is Wolfram Mathematica's `NDsolve[...]`, but packages native to other languages such as SciPy's `integrate.odeint(...)` will achieve the same effect, as demonstrated by [44, 45]. The next sections do not include details of obtaining such solutions, but assumes that the program is capable of numerically solving the MOTSodesic equations and interpolating said results to be analyzed. The code presented will be in pseudo code.

This section concerns the random optimization 'minimum finder' algorithm employed to find MOTS. The algorithm closely follows the sequence laid out in [46].

```
function getRadialDistance(z0)

  initiate, calculate, and set cylindrical solutions 'P(s)' and 'Z(s)'

  find root of the equation 'Z(s)=-z0', set as 's0'
```

```
  return 'P(s)' evaluated at 's=s0'

end function

function samplePosition(std, z0)

  calculate and return a 'z' value sampled from a Gaussian distribution
    with standard deviation 'std' centred at 'z0'

end function

function takeStep(z0, std)

  initiate 'pDist' and set to result of 'getRadialDistance' function
    using 'z0' as argument

  initiate 'newz0' and set to result of 'samplePosition' function
    using 'std' and 'z0' as arguments

  initiate 'newpDist' and set to result of 'getRadialDistance' function
    using 'newz0' as argument

  if 'newpDist' is less than 'pDist', then return 'newz0'

  otherwise return 'z0'

end function

function randomWalker(z0, numsteps, std)

  initiate and set 'newz0' to result of 'takeStep' function
    using 'z0' and 'std' as arguments

  begin loop to loop 'numsteps' times

    set 'newz0' to result of 'takeStep' function
      using 'newz0' and 'std' as arguments

    optionally adapt 'std' to narrow search as loop progresses

    optionally check conditions for quality assurance
```

```
        end loop

    return 'newz0'

end function
```